Comparison of nonreflecting outlet boundary conditions for compressible solvers on unstructured grids

Victor Granet [1]
CERFACS, CFD Team, 42 avenue Gaspard Coriolis, 31057 Toulouse Cedex, France and

Renault SAS, 1 Avenue du Golf, 78288 Guyancourt Cedex, France

Olivier Vermorel[2], Thomas Léonard[3] and Laurent Gicquel[4]
CERFACS, CFD Team, 42 avenue Gaspard Coriolis, 31057 Toulouse Cedex 01, France

Thierry Poinsot[5]
IMFT, Allée Camille Soula, 31400 Toulouse, France

This paper describes extensions and tests of characteristic methods for outlet boundary conditions in compressible solvers. Three methods based on the specification of ingoing waves using one- and multi-dimensional approximations are extended to unstructured grids. They are first compared for weak to strong vortices propagating on low to high speed mean flows through outlet sections. A major issue is to determine the Mach number to be used in the specification of the transverse terms which must be taken into account in the ingoing wave amplitude specifications. For the vortex computations, results show that the averaged Mach number leads to better results than its local value. The boundary conditions are then tested in a more complex case: the flow around a turbine blade. A reference solution using a long distance between the blade trailing edge and the outlet plane is first computed: for this solution, outlet boundary conditions have almost no effect on the flow around the blade. The distance between

---

[1] PhD student, CFD Team CERFACS.
[2] Senior Research Fellow, CFD Team CERFACS.
[3] PhD student, CFD Team CERFACS.
[4] Senior Research Fellow, CFD Team CERFACS.
[5] Research director IMF Toulouse, INP de Toulouse and CNRS. Associate fellow AIAA.

the trailing edge and the outlet plane is then shortened and the various characteristic treatments are compared where intense vortices cross the outlet plane. Results confirm the conclusions obtained on the simple vortex test case.

<div align="center">Nomenclature</div>

C	$=$	chord length
c	$=$	speed of sound
K	$=$	relax coefficient
L_{outlet}	$=$	distance from the outlet section to the blade trailling edge
$\overrightarrow{\mathcal{L}}$	$=$	amplitude vector of the characteristic waves
M_{∞}	$=$	reference Mach number
$M(\overrightarrow{x}, t)$	$=$	local Mach number
$\overline{M}(t)$	$=$	space-averaged Mach number over the outlet section
p_t	$=$	target pressure
$\overrightarrow{\mathcal{R}}$	$=$	residual
$\overrightarrow{\mathcal{R}}^{C}$	$=$	corrected residual
$\overrightarrow{\mathcal{R}}_{in}^{C}$	$=$	incoming corrected residual
$\overrightarrow{\mathcal{R}}^{P}$	$=$	predicted residual
$\overrightarrow{\mathcal{R}}_{in}^{P}$	$=$	incoming predicted residual
$\overrightarrow{\mathcal{R}}_{in,N}^{P}$	$=$	normal contribution of the incoming predicted residual
$\overrightarrow{\mathcal{R}}_{in,T}^{P}$	$=$	transverse contribution of the incoming predicted residual
$\overrightarrow{\mathcal{R}}_{out}^{P}$	$=$	outgoing predicted residual
$\overrightarrow{\mathcal{T}}$	$=$	transverse terms vector
α	$=$	vortex intensity
β	$=$	transverse damping coefficient
Γ	$=$	vortex strength

I. Introduction

Boundary conditions are a usual weak point of compressible solvers especially for Large Eddy Simulations (LES) or Direct Numerical Simulations (DNS) in the subsonic regime. For these unsteady solvers, the capacity to let vortices and acoustic waves leave the domain without generating reflected waves is mandatory but difficult to ensure in multiple applications. To illustrate our objectives, we will consider here two fields of application:

- In CAA (Computational Aero Acoustics), the noise induced by vortices propagating through outlet boundaries can pollute the signal to be measured (the noise created by a jet for example) [1–3]: to avoid this, sophisticated methods to damp vortices before they touch boundaries and to minimize reflection on boundaries must be combined.

- In LES of turbulent flows in confined geometries (combustion chambers for example), acoustic waves created at boundaries by vortices leaving the domain can couple with the flow within the chamber and lead to self-sustained instabilities which are numerical artefacts entirely caused by boundary conditions [4, 5]. Such numerical couplings yield flow predictions which are absolutely stable in the real world into absolutely unstable flow in the simulation world, something which is obviously to avoid.

In both cases, minimizing the reflection level of the boundary is often the most important part of the method. NonReflecting Boundary Conditions (NRBC) for compressible solvers are an old and unsolved research topic [6–8]. All authors agree that characteristic methods based on wave identification must be used. Defining waves for the Navier-Stokes equations is an extremely difficult work in most cases and most authors work only with the Euler equations or assume that the waves found in the Navier-Stokes equations are similar to the inviscid case: two acoustic waves, one entropy wave and two vorticity waves for a nonreacting three-dimensional flow [9]. Viscous terms do not contribute to the wave analysis: they are handled separately. Even when working with the waves corresponding to the inviscid case, the problem remains difficult: while outgoing waves must be computed using interior mesh points, ingoing waves must be specified using boundary conditions. This is where methods differ. It is widely recognized today that at outlets, multidimensional for-

mulations including transverse terms [10–14] provide much better results than the one-dimensional formulations (LODI) proposed by Poinsot et al. for example [9, 15, 16] (this is not the case at inlets where simple LODI formulations give excellent results [17]).

How to build these multidimensional methods and integrate transverse terms into the ingoing wave formulation still is an open topic : low-Mach number expansions [10, 11] show that only a part β , where β is a scalar-valued transverse damping coefficient, of the transverse term should be taken into account and there is no general expression for β except that it should scale like the Mach number.

Our goal in this paper is to improve boundary conditions proposed for example by Yoo et al. [12] or Lodato et al. [14] by extending and testing them in two directions:

- Unstructured meshes: most CAA or DNS studies where characteristic methods have been developed and tested, were performed with finite differences codes using simple structured (i, j, k) meshes. To compute internal flows in piston engines [18] or in gas turbines [19, 20], more complex meshes and methods must be used. The extension of characteristic methods in such geometries requires specific attention and is discussed here.

- Most existing characteristic methods are developed and tested in the linear regime: the usual test for NRBC is a weak vortex of maximum rotation speed U_{max} leaving the domain through an outlet where the convection velocity is U_0 ; tests are performed for $\alpha = U_{max}/U_0 << 1$. In practice, for many geometries, vortices are created by the mean flow (for example in a wake or behind a backward facing step) and propagate towards outlets with high rotational velocities. When these strong vortices interact with outlet boundaries, α is often of order unity. It is important to verify the efficiency of boundary conditions for such conditions and testing NRBC for all vortex strengths is the second objective of this work. It becomes an especially difficult issue when α is larger than unity and local velocities in outlet sections become negative, transforming locally the outlet into an inlet for a limited period of time. In such cases, strong noise may be created but even the robustness of the method may be at stake.

4

The target field of these tests is not CAA for which structured meshes and weak vortices (obtained by adding buffer zones near boundaries) are common practice but rather LES or DNS of confined flows like for example combustion chambers where the boundary condition should be non reflecting over a large range of α.

The paper is organized as follows: first the formalism of Yoo et al. [12] is recalled and its implementation in an unstructured code is described. Second the resulting boundary condition is tested on the convected vortex test case. For this case, the quality of the NRBC is tested by comparing fields of axial velocities, pressure for various mean flow velocities and vortex strengths (up to strong vortices where α is larger than unity). It is shown that multidimensional NRBC formulations of Yoo et al. [12] must be extended in such cases to define which Mach number must be used to evaluate the β parameter required for the transverse terms. Indeed, strong vortices change the mean convection velocity at the outlet: this does not happen for weak vortices which do not modify the mean flow. Finally, an application in a complex geometry, a non-moving turbine blade, is shown to illustrate how the method works in a real configuration. The location of the outlet boundary condition, which is directly linked to the level of perturbations reaching the boundary condition and the number of grid points in the computational domain, is studied. A reference case for which the boundary condition is located far enough from the blade (so that the outlet boundary condition formulation does not affect the solution in the region of interest) is performed. Then, the outlet section is set closer to the blade trailing edge to test the influence of the boundary condition in terms of numerical stability and physical quantities compared to the reference case. Results show on both academic and complex geometry cases that this extended boundary condition allows to let vortices leave the domain with limited acoustic reflection even for strong vortices.

II.   Governing equations

The set of conservation equations describing the evolution of a compressible flow with chemical reactions reads:

$$\frac{\partial \rho}{\partial t} + \frac{\partial}{\partial x_i}\left(\rho u_i\right) = 0 \tag{1}$$

$$\frac{\partial \rho u_j}{\partial t} + \frac{\partial}{\partial x_i}\left(\rho u_i u_j\right) + \frac{\partial p}{\partial x_j} = \frac{\partial \tau_{ij}}{\partial x_i} \tag{2}$$

$$\frac{\partial \rho E}{\partial t} + \frac{\partial}{\partial x_i}\left[u_i\left(\rho E + p\right)\right] = \frac{\partial}{\partial x_i}\left(u_j \tau_{ij}\right) + \frac{\partial}{\partial x_i}\left(q_i\right) + \dot{\omega}_T \tag{3}$$

$$\frac{\partial \rho_k}{\partial t} + \frac{\partial}{\partial x_i}\rho_k\left(u_i + V_i^c\right) = \frac{\partial}{\partial x_i}\left(J_{ki}\right) + \dot{\omega}_k \tag{4}$$

where p is the pressure, ρ is the density of the fluid, $\vec{u} = (u_1, u_2, u_3)$ is the velocity vector, E the total energy per unit mass, $\rho_k = \rho Y_k$ for $k = 1, N$ (N is the total number of species), Y_k is the mass fraction of species k, $\dot{\omega}_T$ is the rate of heat release, $\dot{\omega}_k$ is the reaction rate of species k. The system is closed with the following relations:

- The equation of state for an ideal gas mixture writes:

$$p = \rho r T, \quad r = \sum_{k=1}^{N} Y_k r_k = \sum_{k=1}^{N} Y_k \frac{R}{W_k} = \frac{R}{W}, \quad \frac{1}{W} = \sum_{k=1}^{N} \frac{Y_k}{W_k}$$

where T the temperature and r the gas constant of the mixture which is defined from each species gas constant r_k, R $= 8.13143$ J/K/mol is the universal gas constant, W_k is the molar mass of species k and W is the molar mass of the mixture.

- The viscous stress tensor is expressed as:

$$\tau_{ij} = 2\mu \left[\frac{1}{2}\left(\frac{\partial u_j}{\partial x_i} + \frac{\partial u_i}{\partial x_j}\right) - \frac{1}{3}\delta_{ij}\frac{\partial u_l}{\partial x_l}\right]$$

where μ, the molecular viscosity, is expressed by the Sutherland's law as:

$$\mu = c_1 \frac{T^{(3/2)}}{T + c_2} \frac{T_{ref} + c_2}{T_{ref}^{(3/2)}}$$

where c_1, c_2 and T_{ref} are constants.

- The correction velocity V_i^c, needed to ensure global mass conservation, is:

$$V_i^c = \sum_{k=1}^{N} D_k \frac{W_k}{W}\frac{\partial X_k}{\partial x_i}$$

where X_k is the mole fraction of species k.

- Finally, the diffusive species flux, J_{ki}, and the heat flux, q_i, are:

$$J_{ki} = \rho D_k \frac{W_k}{W} \frac{\partial X_k}{\partial x_i}$$

$$q_i = -\lambda \frac{\partial T}{\partial x_i}$$

where the heat conduction coefficient, λ, and the diffusion coefficient of the species k, D_k, are computed from the viscosity μ as:

$$D_k = \frac{\mu}{\rho S_{c_k}} \qquad \lambda = \frac{\mu C_p}{P_r}$$

where the Schmidt number S_{c_k} is a constant depending on the species and the Prandtl number P_r is assumed to be constant.

III. Navier-Stokes Characteristic Boundary Conditions (NSCBC)

The NSCBC approach [9] uses the Navier-Stokes equations in their characteristic form where outgoing and ingoing waves can be identified. The outgoing waves can be computed from interior points. The ingoing waves, on the other hand, which come from the outside of the domain, must be prescribed to close the boundary problem. In NSCBC, the incoming wave amplitudes are imposed under the LODI assumption. Once all waves are computed, balance equations are used to advance the system in time. Under the LODI assumptions, the flow is assumed to be locally one-dimensional and inviscid.

The limitations of the LODI assumption appear when the flow is three-dimensional at boundaries ; since the flow is not normal to the boundary, the LODI system of equations is not able to handle flow distortions. Nicoud [21] and Yoo et al. [12] demonstrate the importance of taking into account terms corresponding to derivatives which are parallel to the boundary to construct the amplitude of ingoing waves.

The LODI equations on the boundary in their primitive and two-dimensional forms become (viscous,

diffusive terms and body forces are neglected):

$$
\frac{\partial}{\partial t}
\begin{bmatrix}
\rho \\
u_1 \\
u_2 \\
p \\
\rho_k
\end{bmatrix}
+
\begin{bmatrix}
\left(\mathcal{L}_1 + \mathcal{L}_4 + 2\mathcal{L}_2\right)/2c^2 \\
\left(\mathcal{L}_4 - \mathcal{L}_1\right)/2\rho c \\
\mathcal{L}_3 \\
\left(\mathcal{L}_4 + \mathcal{L}_1\right)/2 \\
\mathcal{L}_{4+k}
\end{bmatrix}
+
\begin{bmatrix}
\left(\mathcal{T}_1 + \mathcal{T}_4 + 2\mathcal{T}_2\right)/2c^2 \\
\left(\mathcal{T}_4 - \mathcal{T}_1\right)/2\rho c \\
\mathcal{T}_3 \\
\left(\mathcal{T}_4 + \mathcal{T}_1\right)/2 \\
\mathcal{T}_{4+k}
\end{bmatrix}
=
\begin{bmatrix}
0 \\
0 \\
0 \\
\mathcal{S}_p \\
\mathcal{S}_{\rho_k}
\end{bmatrix}
\tag{5}
$$

where c is the speed of sound and $\overrightarrow{U} = (\rho, u_1, u_2, p, \rho_k)$ is the primitive variable vector. The amplitude vector of the characteristic waves $(\overrightarrow{\mathcal{L}})$ in Eq. (5) is given by:

$$
\overrightarrow{\mathcal{L}} =
\begin{bmatrix}
\mathcal{L}_1 \\
\mathcal{L}_2 \\
\mathcal{L}_3 \\
\mathcal{L}_4 \\
\mathcal{L}_{4+k}
\end{bmatrix}
=
\begin{bmatrix}
\lambda_1\left(\frac{\partial p}{\partial x_1} - \rho c \frac{\partial u_1}{\partial x_1}\right) \\
\lambda_2\left(c^2 \frac{\partial \rho}{\partial x_1} - \frac{\partial p}{\partial x_1}\right) \\
\lambda_3 \frac{\partial u_2}{\partial x_1} \\
\lambda_4\left(\frac{\partial p}{\partial x_1} + \rho c \frac{\partial u_1}{\partial x_1}\right) \\
\lambda_{4+k} \frac{\partial \rho_k}{\partial x_1}
\end{bmatrix}
\tag{6}
$$

where λ_i are the characteristic velocities:

$$
\lambda_1 = u_1 - c, \ \lambda_2 = \lambda_3 = \lambda_{4+k} = u_1, \lambda_4 = u_1 + c
\tag{7}
$$

The transverse terms in their two-dimensional form $(\overrightarrow{\mathcal{T}})$ and the source terms $(\overrightarrow{\mathcal{S}})$ are written as:

$$
\overrightarrow{\mathcal{T}} =
\begin{bmatrix}
\mathcal{T}_1 \\
\mathcal{T}_2 \\
\mathcal{T}_3 \\
\mathcal{T}_4 \\
\mathcal{T}_{4+k}
\end{bmatrix}
=
\begin{bmatrix}
u_2\left(\frac{\partial p}{\partial x_2} - \rho c \frac{\partial u_1}{\partial x_2}\right) + \gamma p \frac{\partial u_2}{\partial x_2} \\
u_2\left(c^2 \frac{\partial \rho}{\partial x_2} - \frac{\partial p}{\partial x_2}\right) + c^2 \rho \frac{\partial u_2}{\partial x_2} - \gamma p \frac{\partial u_2}{\partial x_2} \\
u_2 \frac{\partial u_2}{\partial x_2} + \frac{1}{\rho} \frac{\partial p}{\partial x_2} \\
u_2\left(\frac{\partial p}{\partial x_2} + \rho c \frac{\partial u_1}{\partial x_2}\right) + \gamma p \frac{\partial u_2}{\partial x_2} \\
u_2 \frac{\partial \rho_k}{\partial x_2}
\end{bmatrix}
\tag{8}
$$

$$
\overrightarrow{\mathcal{S}} =
\begin{bmatrix}
\mathcal{S}_p \\
\mathcal{S}_{\rho_k}
\end{bmatrix}
=
\begin{bmatrix}
\dot{\omega}_T \\
\dot{\omega}_k
\end{bmatrix}
\tag{9}
$$

Equation 5 can be written in characteristic form, so called effective boundary conditions by Yoo et al. [12]:

$$
\begin{bmatrix}
\left(\frac{\partial p}{\partial t} - \rho c \frac{\partial u_1}{\partial t} \right) \\
\left(c^2 \frac{\partial \rho}{\partial t} - \frac{\partial p}{\partial t} \right) \\
\frac{\partial u_2}{\partial t} \\
\left(\frac{\partial p}{\partial t} + \rho c \frac{\partial u_1}{\partial t} \right) \\
\frac{\partial \rho_k}{\partial t}
\end{bmatrix}
+
\begin{bmatrix}
\mathcal{L}_1 \\
\mathcal{L}_2 \\
\mathcal{L}_3 \\
\mathcal{L}_4 \\
\mathcal{L}_{4+k}
\end{bmatrix}
+
\begin{bmatrix}
\mathcal{T}_1 \\
\mathcal{T}_2 \\
\mathcal{T}_3 \\
\mathcal{T}_4 \\
\mathcal{T}_{4+k}
\end{bmatrix}
=
\begin{bmatrix}
\mathcal{S}_p \\
-\mathcal{S}_p \\
0 \\
\mathcal{S}_p \\
\mathcal{S}_{\rho_k}
\end{bmatrix}
\tag{10}
$$

For a subsonic outflow, all waves go out except the acoustic wave travelling at the speed $u_1 - c$ corresponding to $\mathcal{L}_1$. $\mathcal{L}_i$ ($i = 2, .., 4 + k$ (5 + k) are directly determined by the expressions in (6). $\mathcal{L}_1$ is computed using (10):

$$
\left(\frac{\partial p}{\partial t} - \rho c \frac{\partial u_1}{\partial t} \right) + \mathcal{L}_1 + \mathcal{T}_1 = \mathcal{S}_p
\tag{11}
$$

The evaluation of the $\mathcal{L}_1$ is a crucial step in the treatment of the boundary condition. Poinsot and Lele [9] prescribed the amplitude of the incoming wave to be fixed at:

$$
\mathcal{L}_1 = K(p - p_t)
\tag{12}
$$

where K is the pressure relaxation coefficient and p_t the target pressure. The form of the coefficient K was proposed by Rudy and Strikwerda [22]:

$$
K = \sigma c \left(1 - M^2 \right) / l_{x_1}
\tag{13}
$$

where M is the maximum Mach number on the boundary, l_{x_1} is the characteristic size of the domain in x_1 direction and σ is a constant usually set to 0.25 [9, 12]. This expression of $\mathcal{L}_1$ makes the boundary condition only partially nonreflecting (if $K \neq 0$) but ensures that the mean pressure remains close to the target pressure p_t. A perfectly nonreflecting boundary condition is obtained when K is set to zero, leading to a zero amplitude of the incoming wave. However, for a perfectly nonreflecting boundary condition, the target pressure often cannot be maintained. Moreover, Eq. (11) often leads to unacceptable reflection at outlets when vortices leave the domain as pointed out by multiple authors [10–14, 23, 24].

Taking into account both works of Yoo et al. [12] who included the transverse contribution in the

expression of $\mathcal{L}_1$ and Sutherland and Kennedy [23] who recognized that the source terms should be neglected, the effective boundary condition can be written as:

$$\left(\frac{\partial p}{\partial t} - \rho c \frac{\partial u_1}{\partial t}\right) + K(p - p_t) + \beta \mathcal{T}_1 = 0 \tag{14}$$

or equivalently:

$$\mathcal{L}_1 = K(p - p_t) + (\beta - 1)\,\mathcal{T}_1 \tag{15}$$

where $\beta \in [0, 1]$ is a transverse damping parameter. When the parameter β is set to one, the LODI assumption is recovered. In the study of Yoo and Im [13], the convected vortex test case presented for $\beta = 1$ shows a tendancy to push the vortex out of the domain too fast. On the other hand, when $\beta = 0$ the boundary seems to resist and damp out the vortex. The most suitable value for β was found, under the low Mach number asymptotic analysis, to be equal to the reference Mach number [13]. This analysis was reported to be also valid for other flows [24].

IV.   Unstructured grid implementation

The ability to distinguish transverse and normal terms is obviously needed in Eq. (10) since their treatment is different. This is a straightforward task on structured grids where boundaries are usually one of the mesh planes (i, j or k constant); however, on unstructured grids, this is not the case anymore. Indeed, on unstructured grids, the boundary can be composed of edges of various elements. This section presents (1) how to estimate the transverse terms $\overrightarrow{\mathcal{T}}$ presented in Eq. (8) and (2) a practical implementation in a subsonic compressible code.

Using the cell-vertex formalism, the quantity which is actually used is the nodal residual $\overrightarrow{\mathcal{R}}_i^n$ ($\overrightarrow{\mathcal{R}}$). The relationship between this residual and the quantities of interest, $\overrightarrow{\mathcal{L}}$ and $\overrightarrow{\mathcal{T}}$, is presented in Appendix A. Knowing the vector of primitive variables $\overrightarrow{V}^n$ at time t, the vector $\overrightarrow{V}^{n+1}$ at time $t + \Delta t$ is computed for each node i as:

$$\overrightarrow{V}_i^{n+1} = \overrightarrow{V}_i^n - \frac{\Delta t}{V_i}\overrightarrow{\mathcal{R}}_i^n \tag{16}$$

$$(\overrightarrow{V}^{n+1} = \overrightarrow{V}^n - \frac{\Delta t}{V_i}\overrightarrow{\mathcal{R}}_i^n)$$

where V_i is the nodal volume around node i and $\overrightarrow{\mathcal{R}}_i^n$ is the nodal residual at node i computed by the numerical scheme.

The outlet-boundary nodal residual $\overrightarrow{\mathcal{R}}_i^n$ needs to be corrected on all nodes which are on the boundary. For this, using Eq. (5), the residual $\overrightarrow{\mathcal{R}}^P$ predicted by the numerical scheme is first decomposed as:

$$
\overrightarrow{\mathcal{R}}^P = \overrightarrow{\mathcal{R}}_{in}^P + \overrightarrow{\mathcal{R}}_{out}^P =
\begin{pmatrix}
\frac{\mathcal{L}_1 + \mathcal{T}_1}{2c^2} \\[2mm]
-\frac{\mathcal{L}_1 + \mathcal{T}_1}{2\rho c} \\[2mm]
0 \\[2mm]
\frac{\mathcal{L}_1 + \mathcal{T}_1}{2} \\[2mm]
0
\end{pmatrix}
+
\begin{pmatrix}
\frac{2[\mathcal{L}_2 + \mathcal{T}_2] + \mathcal{L}_4 + \mathcal{T}_4}{2c^2} \\[2mm]
\frac{\mathcal{L}_4 + \mathcal{T}_4}{2\rho c} \\[2mm]
\mathcal{L}_3 + \mathcal{T}_3 \\[2mm]
\frac{\mathcal{L}_4 + \mathcal{T}_4}{2} \\[2mm]
\mathcal{L}_{4+k} + \mathcal{T}_{4+k}
\end{pmatrix}
\tag{17}
$$

To compute the corrected values of the residual $\overrightarrow{\mathcal{R}}^C$ which will replace $\overrightarrow{\mathcal{R}}^P$, the normal and transverse parts of $\overrightarrow{\mathcal{R}}_{in}^P$ $(\mathcal{R}_{in}^P)$ are first computed. Using the cell-vertex formalism, two different strategies can be used: (1) an exact strategy would be to use the numerical scheme on the normal and transverse part of the variables to estimate the normal and transverse residuals. However, this method is not retained as it is too expensive in terms of both CPU cost and memory requirement. Therefore, (2) the transverse part is estimated while computing the divergence of the transverse flux on all cells which have a node on the boundary [25]:

$$
\overrightarrow{\mathcal{R}}_{in,T}^P|_{cell} = \overrightarrow{\nabla} \cdot \overrightarrow{\mathcal{F}} = -\frac{1}{DV_c} \left(\sum_{j \in \Omega_c} \left[\overrightarrow{\mathcal{F}}_j - \left(\overrightarrow{\mathcal{F}}_j \cdot \overrightarrow{n}_i \right) \overrightarrow{n}_i \right] \cdot \overrightarrow{N}_j \right)
\tag{18}
$$

where $\overrightarrow{\mathcal{F}} = \left(\overrightarrow{F}, \overrightarrow{G}, \overrightarrow{H} \right)$ is the flux ($\overrightarrow{F}$, $\overrightarrow{G}$ and $\overrightarrow{H}$ are defined in Appendix A), D is the number of dimension, V_c is the volume of the cell Ω_c, Ω_c is each cell with a vertex j on the boundary patch, n_i is the inward normal to each node i of the boundary patch, N_j is the outward normal to each vertex j of the cell Ω_c.

The transverse part of the residual on node i, $\overrightarrow{\mathcal{R}}_{in,T}^P$ $(\mathcal{R}_{in,T}^P)$, is then recovered by scattering the weighted residual on the cells c surrounding this node:

$$
\overrightarrow{\mathcal{R}}_{in,T}^P = \frac{1}{V_i} \sum_{c, i \in \Omega_c} \left(\frac{V_c}{I_c} \overrightarrow{\mathcal{R}}_{in,T}^P|_{cell} \right)
\tag{19}
$$

where $V_i = \sum_{c, i \in \Omega_c} \frac{V_c}{I_c}$ and I_c is the number of nodes in each cell. The normal contribution is then

retrieved:

$$\overrightarrow{\mathcal{R}}_{in,N}^{P} = \overrightarrow{\mathcal{R}}_{in}^{P} - \overrightarrow{\mathcal{R}}_{in,T}^{P} = \begin{pmatrix} \frac{\mathcal{L}_1}{2c^2} \\[1em] -\frac{\mathcal{L}_1}{2\rho c} \\[1em] 0 \\[1em] \frac{\mathcal{L}_1}{2} \\[1em] 0 \end{pmatrix} \tag{20}$$

which leads to the decomposition:

$$\overrightarrow{\mathcal{R}}^{P} = \overrightarrow{\mathcal{R}}_{in,N}^{P} + \overrightarrow{\mathcal{R}}_{in,T}^{P} + \overrightarrow{\mathcal{R}}_{out}^{P} \tag{21}$$

To evaluate the corrected residual $\overrightarrow{\mathcal{R}}^{C}$, this incoming predicted contribution $\overrightarrow{\mathcal{R}}_{in,N}$ is removed from the residual $\overrightarrow{\mathcal{R}}^{P}$ while the corrected contribution $\overrightarrow{\mathcal{R}}_{in}^{C}$ is added:

$$\overrightarrow{\mathcal{R}}^{C} = \overrightarrow{\mathcal{R}}^{P} - \overrightarrow{\mathcal{R}}_{in,N}^{P} + \overrightarrow{\mathcal{R}}_{in}^{C} \tag{22}$$

where $\overrightarrow{\mathcal{R}}_{in}^{C}$ is written as:

$$\overrightarrow{\mathcal{R}}_{in}^{C} = \begin{pmatrix} \frac{K(p-p_t)-(1-\beta)\mathcal{T}_1}{2c^2} \\[1em] -\frac{K(p-p_t)-(1-\beta)\mathcal{T}_1}{2\rho c} \\[1em] 0 \\[1em] \frac{K(p-p_t)-(1-\beta)\mathcal{T}_1}{2} \\[1em] 0 \end{pmatrix} \tag{23}$$

The effective boundary condition on the incoming wave then corresponds to the one obtained in Eq. (14). The final equation can also be written as:

$$\overrightarrow{V}_i^{n+1} = \overrightarrow{V}_i^{n} - \frac{\Delta t}{V_i} \left[\overrightarrow{\mathcal{R}}^{P} - \overrightarrow{\mathcal{R}}_{in,N}^{P} + \overrightarrow{\mathcal{R}}_{in}^{C} \right] \tag{24}$$

$$(\overrightarrow{V}^{n+1} = \overrightarrow{V}^{n} - \frac{\Delta t}{V_i} \left[\overrightarrow{\mathcal{R}}^{P} - \overrightarrow{\mathcal{R}}_{in}^{P} + \overrightarrow{\mathcal{R}}_{in}^{C} \right])$$

The code used here works with the conservative variables which are retrieved by multiplying Eq. (24) by a transformation matrix noted A^{-1} (cf. Appendix A for details).

V. Results

Computations are performed with the AVBP solver. This Computational Fluid Dynamic (CFD) solver is a fully 3D code solving the unsteady, compressible, multi-species Navier-Stokes equations

on unstructured grids using the cell-vertex finite volume approximation [26]. For the present study, a two-step Taylor Galerkin numerical scheme [16, 27] is chosen, providing a third-order accuracy in space and time.

A.   Convected Vortex

To evaluate the ability of the nonreflecting boundary condition ($K = 0$ in Eq. (15)) to handle outgoing vortices, a typical convected vortex case [9, 14] is first performed. A single vortex is superimposed on a homogeneous flow field and is convected through the outlet boundary condition. The stream function, ψ, of the initial vortex is defined as:

$$\psi(x_1, x_2) = \Gamma e^{\frac{(x_1 - x_{1c})^2 + (x_2 - x_{2c})^2}{2R_c^2}} \tag{25}$$

where Γ is the vortex strength, (x_{1c}, x_{2c}) are the coordinates of the vortex center and R_c is the radius of the vortex. The velocity field and the maximum velocity induced by the vortex are given by:

$$u_1 = \frac{\partial \psi}{\partial x_2}, \quad u_2 = -\frac{\partial \psi}{\partial x_1}, \quad U_{max} = \frac{\Gamma}{R_c \sqrt{e}} \tag{26}$$

The corresponding initial pressure field is given by:

$$p - p_\infty = -\frac{\rho \Gamma^2}{2R_c^2} e^{\frac{(x_1 - x_{1c})^2 + (x_2 - x_{2c})^2}{R_c^2}} \tag{27}$$

where p_∞ is the reference pressure.

The computational domain is a square of dimension $L = 0.013m$ to match the configuration used in [14] with 40 grid points in each direction. The reference pressure and temperature are $101300Pa$ and $300K$ respectively, and the gas is nitrogen. The initial vortex is added to a uniform mean flow of velocity U_0. It is located at the center of the domain so that $(x_{1c}, x_{2c}) = (0, 0)$. Its radius is set to $0.0013m$, which is 10% of the box size L. A periodicity condition is applied to bottom and top boundaries to avoid corner issues discussed by Lodato et al. [14].

Most authors indicate that the damping parameter β should be of the order of the Mach number [13, 14, 24]. The difficult question is to know which Mach number should be used, especially in flows where the outlet velocity field changes significantly both with time and position. Yoo and Im [13]

13

used a constant reference Mach number $M = M_\infty$ for their tests. However, this definition is not well-suited for complex flows where the Mach number can locally vary within a wide range of values and choosing a mean "reference" Mach can be difficult (typically a high speed jet crossing a boundary). Lodato et al. [14] chose the reference Mach number for their vortex test case, $\beta = M_\infty$, and the maximum Mach number over the whole domain for their spherical pressure wave test. In the present work, two different strategies are tested for the damping parameter:

- $\beta = \beta(\overrightarrow{x}, t) = M(\overrightarrow{x}, t) = \frac{u_1(\overrightarrow{x}, t)}{c(\overrightarrow{x}, t)}$: using a local Mach number on the boundary nodes allows to take into account velocity variations on the boundary.

- $\beta = \beta(t) = \overline{M}(t) = \overline{\left(\frac{u_1(\overrightarrow{x}, t)}{c(\overrightarrow{x}, t)} \right)}$: using a mean Mach number averaged in space over the exit section on the boundary nodes combines the advantages of the two options M_∞ and $M(\overrightarrow{x}, t)$.

Note that in the above expression, $\overline{(.)}$ denotes an average over the exit section. The three boundary conditions analysed in this paper are presented in Table 1.

To analyse their performance, four different cases are performed (Table 2). Cases A and B are two

	Name	β
BC1	Poinsot and Lele [9]	1
BC2	Yoo et al. extension [12]	$M(\overrightarrow{x}, t)$
BC3	Yoo et al. extension [12]	$\overline{M}(t)$

Table 1 Tested boundary conditions. The parameter β controls the level of integration of the transverse terms in the ingoing wave: $\mathcal{L}_1 = K(p - p_t) + (\beta - 1)\mathcal{T}_1$ (Eq. (15)).

Case	U_0 $(m.s^{-1})$	M_∞	Γ $(m^2.s^{-1})$	$\alpha = U_{max}/U_0 (\%)$
A	10	0.028	0.011	50
B	10	0.028	0.066	300
C	100	0.28	0.11	50
D	100	0.28	0.022	100

Table 2 Convected vortex parameters.

cases at low Mach number (0.028) while cases C and D are performed for a mean Mach number which is ten times higher (0.28). Case A presents the evolution of a weak vortex ($\alpha < 1$). A very

strong vortex ($\alpha > 1$) is performed in case B where the maximum velocity induced by the vortex is three times higher than the mean velocity. The flow at the boundary will thus locally switch from outcoming to incoming.

Figures 1 to 8 display normalized pressure and velocity fields illustrating the performances of the three conditions BC1, 2 and 3 for the four test cases of Table 2. The normalized pressure field p^* is defined using the initial pressure at the vortex center $p(0,0)$:

$$p^*(\overrightarrow{x}, t^*) = \frac{p(\overrightarrow{x}, t^*) - p_\infty}{p(0,0) - p_\infty} = -(p(\overrightarrow{x}, t^*) - p_\infty)\frac{2R_c^2}{\rho\Gamma^2} \qquad (28)$$

where t^* is a dimensionless time given by $t^* = t/\tau$ with $\tau = L/2U_0$: i.e. the vortex begins to interact with the outlet boundary around $t^* = 0.5$ and leaves the domain at $t^* = 1.0$.

Figures 1, 3, 5 and 7 show isocontours of the axial velocity and normalized pressure fields in gray scale. These figures present early moments of the simulation (t^*=0, 0.45, 1.12 and 1.43) to analyse the evolution of the vortex when it leaves the box. More quantitative comparisons of methods BC1, 2 and 3 are given using one-dimensional profiles along the right boundary (i.e. $x_1 = L/2$) in Figs. 2, 4, 6 and 8 once the vortex has left the domain at dimensionless times 1.25, 1.5 and 1.75. These are the most critical instants for the simulation because the vortex has left the domain almost completely and any perturbation due to the boundary condition appears clearly. Finally, the temporal evolution of the normalized mean pressure in the whole domain as a function of the dimensionless time t^* is given in Fig. 9.

Spatial evolutions

Low Mach Number (M_∞=0.028): Cases A and B

Figures 1 and 3 compare the effect of the velocity induced by the vortex on the boundary condition for a low-speed mean flow. For this case, the parameters of the strong vortex are set such that the mean convection velocity sign is changed (for instance for case B, the induced velocity ranges from 40m/s to -20m/s so that the outlet can be an inlet for a short period of time when the vortex leaves the domain. First, for both a weak (case A, $\alpha = 50\%$) and a strong (case B, $\alpha = 300\%$) vortex, the LODI assumption (BC1) is not able to handle the distortions induced by the vortex.

For a weak vortex, in Fig. 1, the reflections at the boundary are significant and the axial velocity isocontours are very disturbed. For a strong vortex, Fig. 3 shows that the boundary condition fails to let the vortex leave the domain correctly. The simulations performed with BC2 exibit an intriguing behavior: on the one hand, the axial velocity isocontours are not really perturbed but on the other hand, the pressure is very disturbed: when the vortex reaches the boundary, the pressure drops below the mean value (at $t^* = 1.12$ on both Fig. 1 and Fig. 3) and then starts to recover. Such instabilities have already been mentioned by Yoo and Im [13]. When the BC3 method is used however, no such behavior is observed. Neither the velocity isocontours nor the pressure field are affected when the vortex reaches the boundary. Figures 2 and 4 are plotted at times further away from $t^* = 1$ to check the pressure levels in the computational domain after the vortex has left the domain. In Figs. 2 and 4, at $t^* = 1.25$, simulations with BC3 give excellent results compared to the analytical solution. Even if the axial velocity changes sign and becomes negative, the boundary is still able to handle the vortex. As observed in the 2D fields, Figs. 2 and 4 show that BC1 results deviate strongly from the analytical solution (solid line). The symmetry of the velocity profile is already lost even for the weak vortex in Fig. 2. At $t^* = 1.5$ in Fig. 2, the vortex has left the domain, but BC1 is still oscillating whereas BC2 and 3 are close to the mean pressure. However, in Fig. 4, BC3 is the only method for which pressure has recovered its analytical value. The pressure field is also homogeneous for BC2 but its value (~ -0.16) has drifted from the expected value. At $t^* = 1.75$, for the strong vortex (Fig. 4) the LODI simulation fails earlier and is not represented here. At this time the vortex has left the domain, Figs. 2 and 4 confirm that only the BC3 method using $\beta = \overline{M}(t)$ is able to recover the mean pressure of the flow.

High Mach Number (M_∞=0.28): Cases C and D

Figures 5 and 7 present the results for cases C and D where M_∞ is ten times higher than for cases A and B. Interestingly, for these cases, the classical LODI assumption (BC1) gives quite good results compared to the ones obtained with a lower M_∞ (Fig. 1 to 4). The distortions of the axial velocity isocontours in Fig. 5 are less important for case C than those observed in Figs. 1 and 3. This result is coherent with the original paper of Poinsot and Lele [9] where

the LODI assumption gave excellent results for a vortex convected on a mean flow which was supersonic. Lodato et al. [14] also performed simulations with a mean Mach number up to 0.8 using the LODI assumption. On their Fig. 8, the velocity isocontours are not disturbed while using such a high mean Mach number. When BC2 is used, case A shows a large variation of the pressure after the vortex has reached the boundary. However, this is not observed here, or at least in much smaller proportions, for cases C and D. Distortions of the velocity isocontours are not observed in both cases. Finally, BC3 gives excellent results for both cases. At all times plotted in Figs. 6 and 8 the distortions generated on the pressure field while using the LODI assumption appears to oscillate. At $t^* = 1.25$, on both Figs. 6 and 8 the values of the axial velocity for the LODI assumption already started to drift away from the analytical solution.

Temporal evolutions

Figure 9 summarizes the results for the vortex test case by plotting the mean pressure in the whole domain nondimensionalized by its initial value as a function of time for all cases. For the weak vortices (left column), the BC1 runs (triangles) experience a very high peak around $t^* = 1$ for both cases and then hardly manage to reach $p^* = 0$ even at $t^* = 4$. This confirms that strong acoustic reflections are generated when the vortex leaves and that the flow needs a long time to recover. A smaller peak for case A is seen by the use of BC2. BC3 fits the analytical solution well and does not generate spurious reflections. For strong vortices (right column), the conclusions are similar: BC1 fails to compute case B (the code stops because of nonphysical (*non physical*) values for temperature). The simulation performed with BC2 presents a peak before the vortex reaches the boundary ($t^* = 0.8$) and then underestimates the pressure evolution. BC3 handles this critical vortex very well.

B.   Turbine blade

In the wake of a turbine blade, strong vortices are produced. These vortices, when reaching the outlet boundary condition, may lead to large spurious reflections which can perturb the flow along the blade. This flow is therefore a good prototype to test outlet boundary conditions in a more

realistic case than the usual vortex flow. Of course, extending the domain far downstream of the blade is a solution to minimize the effects of the outlet boundary condition so that, when setting up the location of the outlet boundary condition of such a simulation, two conflicting requirements must be satisfied: (1) limit the size of the computational domain to reduce the CPU time and (2) ensure that the reflections induced by the boundary condition do not affect the flow along the blade. The ability of boundary conditions BC1 to 3 to fulfill these two requirements is assessed in this section.

Configuration

The configuration corresponds to the blade studied experimentally by Sieverding et al. [28, 29] (Table 3). The computation is performed in two dimensions. This is sufficient to evaluate the

Chord length	140 mm
Axial chord length	91.8 mm
Trailing edge diameter	7.4 mm
Inlet angle (from axial direction)	0°

Table 3 Blade characteristic dimensions.

effects of boundary conditions. Moreover, even though a detailed comparison with the experiment is out of scope for the present study, the agreement between experimental data and the present LES is actually very good (as shown below) suggesting that three dimensional effects have a second order influence on the flow statistics.

Figure 10 shows the reference 2D computational domain where the outlet boundary condition is located 10 chords away from the blade trailing edge where a chord, noted C, is the length of the blade. The inlet boundary condition imposes a total pressure and a total temperature. The inlet Mach number is equal to 0.19 and its associated Reynolds number is about 2.8×10^6. Both top and bottom boundary conditions are set as periodic. The outlet boundary condition is switched between the three boundary conditions previously mentioned in section V A. However, unlike the academic vortex test, an outlet pressure must be maintained. To do so, the relax parameter K in Eq. (15) is not null like for the vortex test case but set to $K = 500 s^{-1}$ so that the

18

boundary condition is quasi-nonreflective. The simulated case is not very sensitive to the value of the relax parameter: tests (not shown here) with reasonable changes for K from $200s^{-1}$ to $1000s^{-1}$ lead to the same conclusions. Note that the location of the probe placed in the wake of the blade used to analyse the signals of each simulations is represented by a cross in Fig. 10.

Impact of the location of the outlet boundary condition

On such a complex geometry, special care is needed to isolate the influence of the boundary condition. Unlike the vortex test case, multiple vortices are continuously created at the blade trailing edge and no analytical solution is available. In order to get a reference simulation, the outlet boundary condition is first placed far away from the blade trailing edge ($L_{outlet}/C = 10$). At this distance, the flow is homogeneous and gradients are null. In other words, for this "reference" simulation the three BCs should be equivalent.

Reference case: $L_{outlet}/C = 10$

Figure 10 top shows the computational grid while Fig. 10 bottom shows an instantaneous field of $\nabla \rho$. The vortices generated in the wake of the blade remain quite strong right after the blade trailing edge. As expected, 10 chords away from the blade trailing edge, the perturbations reaching the outlet boundary condition are very small. Figure 11 shows the time-averaged isentropic Mach distribution along the blade wall and the time-averaged pressure distribution along the blade trailing edge for this reference simulation using BC1, 2 or 3. The experimental mean isentropic Mach distribution agrees extremely well with the ones predicted by the simulations. Moreover, the formalism used for outlet boundary condition has no impact on the simulations validating the fact that this simulation can be used as a reference for other simulation performed with shorter outlets. To quantify the intensity of vortices shed behind the blade, spatial-averages of the time-averaged Root Mean Square (RMS) pressure at various axial locations are calculated for the reference case (Table 4). An estimation of the α parameter introduced for the vortex case (the vortex rotation speed normalized by the average flow speed) is also given. As expected, the level of perturbation increases while getting closer to the blade trailing edge. The perturbations at $x_1/C = 1$ are almost

19

Cutting plane position (x_1/C)	1	1.5	2	3	5	8	10
P_{RMS} (Pa)	4154	2362	1617	1161	872	832	765
$\alpha = U_{max}/U_0$ (%)	141	80	45	< 5	< 5	< 5	< 5

Table 4 Spatial-average value of the time-averaged RMS pressure and of the α parameter at different cutting planes for the reference simulation ($L_{outlet}/C = 10$).

3 times higher than the one experienced at $x_1/C = 2$: the vortices shed behind the blade (Fig.10) are dissipated rapidly, not only because of turbulent dissipation but also because the grid becomes coarser after $x_1/C = 1$ (Fig. 10 top). The objective here is not to compute the evolution of vortices in this zone but to make sure that they do not affect the pressure distribution on the blade. Note however, that the vortex rotation speed (measured by α) increases rapidly when x_1/C decreases: at $x_1/C = 1$ the vortices are so intense ($\alpha = 140\%$) that the sign of the velocity normal to the cutting plane changes. For simulations with smaller domains ($L_{outlet}/C = 1$ or 2), the outlet boundary condition has to handle strong vortices and even negative velocities, similarly to the vortex test case of Section V A.

Once the reference simulation is available, the strategy is then to move the location of the outlet boundary condition closer to the blade trailing edge and repeat the simulation. Preliminary simulations (not shown here) at various positions with the three BCs have shown that BC1 is not able to let the simulation run when the outlet boundary condition is brought closer than 2 chords from the blade trailing edge (position b in Fig. 10 corresponding to $L_{outlet}/C = 2$): BC1 fails between 1 and 2 chords away from the blade trailing edge because it cannot handle vortices which are more intense than the ones experienced at 2 chords (Table 4). On the other hand, BC2 and BC3 let the simulation run for all lengths of the exhaust duct L_{outlet} (down to 1 chord away from the blade trailing edge) confirming their beneficial effect on stability: these boundary conditions allow the simulation to run even when very high level of perturbations are encountered at the outlet. To highlight the influence of each BC on the simulation, two characteristics locations are retained to present the results:

- 2 chords (position b in Fig. 10): a typical location for the outlet boundary condition for such simulations and the closest location to the blade trailing edge where the three BCs are able

20

to let the simulation run.

- 1 chord (position c in Fig. 10): used to discriminate BC2 and BC3 and the closest location which ensures that no physical phenomenon (such as vortex shedding for instance) is removed from the analysis.

Comparison of BC1, BC2 and BC3 for $L_{outlet}/C = 2$

Figure 12 shows the mean isentropic Mach distribution along the blade wall and the mean pressure distribution along the blade trailing edge for all BCs when the exhaust duct length is shortened to $L_{outlet}/C = 2$. Strong vortices cross this section ($\alpha = 45$ ($\alpha = 80$)) but the velocity is always outgoing (the outlet remains an outlet at all times). The fields measured at the outlet of this simulation are compared to the fields obtained at $x_1/C = 2$ in the reference simulation ($L_{outlet}/C = 10$). All BCs reproduce the reference case qualitatively but some discrepancies are observed. On both graphs, BC3 results are closer to the reference case (solid line). Figure 13 presents the temporal evolution of the pressure recorded at the probe (the position of the probe is marked by a cross in Fig. 10 and remains at the same position for all simulations). Here, BC1 differs from both BC2 and BC3: BC1 leads to high pressure fluctuations due to higher spurious reflections on the outlet. Both BC2 and BC3 present levels of pressure fluctuations matching the reference case. Table 5 shows the spatial-average value of the time-averaged RMS pressure in a cutting plane located at 1.5 chords.

The deviation presented by BC1 from the reference case is very large. BC2 and BC3 are close to

	Reference ($L_{outlet}/C = 10$)	BC1 ($L_{outlet}/C = 2$)	BC2 ($L_{outlet}/C = 2$)	BC3 ($L_{outlet}/C = 2$)
P_{RMS} (Pa)	2362	4142	2785	2447

Table 5 Spatial-average value of the time-averaged RMS pressure in a cutting plane located at 1.5 chords for the reference case ($L_{outlet}/C = 10$), and the 2 chords simulations ($L_{outlet}/C = 2$) using BC1, BC2 and BC3.

the reference case even if BC3 agrees better with the levels calculated with the reference case.

Comparison of BC2 and BC3 (BC1 fails) for $L_{outlet}/C = 1$

When the computational domain is shortened again to position c in Fig. 10, the outlet boundary condition is hit by very strong vortices ($\alpha = U_{max}/U_0$ of the order of 140%, Table 4) which can even lead to locally ingoing velocities, a difficult test for boundary conditions. BC2 and BC3 allow the simulation to run but BC1 fails. The previous quantities of interest along the blade are examined again in Fig 14. BC2 results are strongly perturbed. The isentropic Mach number profile on the blade does not match the reference case result. The flow is supersonic along almost half of the suction side (*extrados*) of the blade while the reference case is mostly subsonic. In this particular configuration, the physics of the simulation around the blade are changed by the formalism of the outlet boundary condition, leading to non physical results. On the other hand, BC3 remains close to the values predicted by the reference case and the overall profile is the same. For this case where strong vortices impact the outlet section, the results obtained in simple test cases (Section V A) are recovered: the best solution is to use a coefficient β in the transverse terms given by the averaged Mach on the outlet section ($\beta = \overline{M}(t)$). The other methods lead either to a blow up of the simulation (BC1, the original LODI formulation) or to nonphysical results (BC2 where the local Mach number is used for β).

VI.   Conclusions

The two objectives of this paper are (1) to show how characteristic methods, usually developed for solvers using (i, j, k) structured grids, can be extended to arbitrary unstructured meshes based on cell-vertex residual methods and (2) to check how such boundary conditions perform when strong vortices, inducing large changes of outlet normal velocity and even negative outlet speeds, are convected through the boundary. These questions are crucial for Large Eddy Simulation of compressible flows where vortices leaving the computational domain do not have to be weak as in most academic studies of boundary conditions and can induce very large outgoing speed changes. Three nonreflecting boundary conditions are tested for a vortex of maximum rotation speed U_{max} convected through a subsonic outlet at an average velocity U_0: BC1, the classical Local One-Dimensional Inviscid (LODI) Navier-Stokes Characteristics Boundary Conditions (NSCBC) method,

and two three-dimensional extensions of the LODI method: BC2, where the Mach number used to evaluate the damping coefficient, β, of the additional transverse terms is the local instantaneous Mach number at each point of the outlet and BC3, where the β term is evaluated from the space-averaged value of the Mach number on the outlet section. Obviously, for very weak vortices convected by a high-speed flow ($\alpha = U_{max}/U_0 << 1$), BC2 and BC3 would be equivalent. However, when α increases, this is no longer true and results show that in all cases, BC3 performs better than BC2. For all tests, BC2 and BC3 which include transverse terms in the evaluation of the ingoing wave, perform better than the usual one-dimensional LODI (BC1) method even though tests show that this method gives reasonable results when the mean outlet Mach number is large enough, thereby confirming why previous authors found LODI to be appropriate when they performed tests in high-speed flows. The three boundary conditions are then tested on a complex geometry case: a turbine blade. For this flow, vortices are constantly generated at the blade trailing edge and impact the outlet section with high rotational speeds making the choice of the boundary condition crucial. A reference run is performed by using a very long domain (10 chords) where vortices are dissipated before they reach the outlet. Two shorter domains (two and one chords) are then tested to investigate the responses of BC1, 2 and 3 to vorticity perturbations reaching the boundary. The same hierarchy as the vortex case is reported for BC1, BC2 and BC3: BC1 was not able to handle high levels of perturbations whereas BC2 and BC3 performed well even for shorter domains and high levels of perturbation. However, BC3 provides the best agreement with the reference solution, showing that the current choice for the β coefficient is the averaged value of the Mach number on the outlet section.

Appendix A

While neglecting viscous, diffusive terms and body forces, Eqs. (2) - (4) can be written in matrix notation:

$$\frac{\partial \overrightarrow{U}}{\partial t} + \frac{\partial \overrightarrow{F}}{\partial x_1} + \frac{\partial \overrightarrow{G}}{\partial x_2} + \frac{\partial \overrightarrow{H}}{\partial x_3} = 0 \qquad (29)$$

where $\vec{U}$ is the vector of conserved variables $\vec{U} = [\rho u_1, \rho u_2, \rho u_3, \rho E, \rho_k]^t$. The fluxes in x_1, x_2 and x_3 directions are:

$$\vec{F} = \left[\rho u_1 u_1 + \boxed{\mathrm{p}}\,(P), \rho u_2 u_1, \rho u_3 u_1, \rho H u_1, \rho_k u_1 \right]^t \tag{30}$$

$$\vec{G} = \left[\rho u_1 u_2 + \boxed{\mathrm{p}}\,(P), \rho u_2 u_2, \rho u_3 u_2, \rho H u_2, \rho_k u_2 \right]^t \tag{31}$$

$$\vec{H} = \left[\rho u_1 u_3 + \boxed{\mathrm{p}}\,(P), \rho u_2 u_3, \rho u_3 u_3, \rho H u_3, \rho_k u_3 \right]^t \tag{32}$$

where H is the total enthalpy as: $\rho H = \rho E + \boxed{\mathrm{p}}\,(P)$.

Three transformation matrices A, A_Ω and B (Table 6) are needed to transform the vector of conservative variables $\vec{U}$ into the vector containing the characteristic wave amplitudes' $\vec{\mathcal{L}}$:

$$C = A A_\Omega B \tag{33}$$

with:

$$\vec{U} = C \vec{\mathcal{L}} \tag{34}$$

$(\vec{i}, \vec{j}, \vec{k})$				$(\vec{n}, \vec{t}_1, \vec{t}_2)$		
$\partial \vec{U}$		$\partial \vec{V}$		$\partial \vec{V}_n$		$\vec{\mathcal{L}}$
$\begin{pmatrix} \partial(\rho u_1) \\ \partial(\rho u_2) \\ \partial(\rho u_3) \\ \partial(\rho E) \\ \partial \rho_k \end{pmatrix}$	$\begin{array}{c} A \\ \rightarrow \\ \leftarrow \\ A^{-1} \end{array}$	$\begin{pmatrix} \partial u_1 \\ \partial u_2 \\ \partial u_3 \\ \partial p \\ \partial \rho_k \end{pmatrix}$	$\begin{array}{c} A_\Omega \\ \rightarrow \\ \leftarrow \\ A_\Omega^{-1} \end{array}$	$\begin{pmatrix} \partial u_n \\ \partial u_{t_1} \\ \partial u_{t_2} \\ \partial p \\ \partial \rho_k \end{pmatrix}$	$\begin{array}{c} B \\ \rightarrow \\ \leftarrow \\ B^{-1} \end{array}$	$\begin{pmatrix} (u_n + c)\left(\frac{\partial u_n}{\partial n} + \frac{1}{\rho c} \frac{\partial p}{\partial n} \right) \\ (u_n - c)\left(-\frac{\partial u_n}{\partial n} + \frac{1}{\rho c} \frac{\partial p}{\partial n} \right) \\ u_n \frac{\partial u_{t_1}}{\partial n} \\ u_n \frac{\partial u_{t_2}}{\partial n} \\ u_n \left(\frac{\partial \rho_k}{\partial n} - \frac{Y_k}{c^2} \frac{\partial p}{\partial n} \right) \end{pmatrix}$

Table 6 Summary of the transformation matrices.

The three matrices A, A_Ω and B are expressed as:

$$A = \begin{pmatrix} \frac{1}{\rho} & 0 & 0 & 0 & -\frac{u_1}{\rho} & \cdots & -\frac{u_1}{\rho} \\ 0 & \frac{1}{\rho} & 0 & 0 & -\frac{u_2}{\rho} & \cdots & -\frac{u_2}{\rho} \\ 0 & 0 & \frac{1}{\rho} & 0 & -\frac{u_3}{\rho} & \cdots & -\frac{u_3}{\rho} \\ -\hat{\gamma}(\beta)u_1 & -\hat{\gamma}(\beta)u_2 & -\hat{\gamma}(\beta)u_3 & \hat{\gamma}(\beta) & \hat{\gamma}(\beta)e_c + \chi_1 & \cdots & \hat{\gamma}(\beta)e_c + \chi_k \\ 0 & 0 & 0 & 0 & 1 & \cdots & 0 \\ \vdots & \vdots & \vdots & \vdots & \vdots & \ddots & \vdots \\ 0 & 0 & 0 & 0 & 0 & \cdots & 1 \end{pmatrix} \tag{35}$$

$$A_\Omega = \begin{pmatrix} n_x & n_y & n_z & 0 & 0 & \cdots & 0 \\ t_{1_x} & t_{1_y} & t_{1_z} & 0 & 0 & \cdots & 0 \\ t_{2_x} & t_{2_y} & t_{2_z} & 0 & 0 & \cdots & 0 \\ 0 & 0 & 0 & 1 & 0 & \cdots & 0 \\ 0 & 0 & 0 & 0 & 1 & \cdots & 0 \\ \vdots & \vdots & \vdots & \vdots & \vdots & \ddots & \vdots \\ 0 & 0 & 0 & 0 & 0 & \cdots & 1 \end{pmatrix} \tag{36}$$

$$B = \begin{pmatrix} 1 & 0 & 0 & \frac{1}{\rho c} & 0 & \cdots & 0 \\ -1 & 0 & 0 & \frac{1}{\rho c} & 0 & \cdots & 0 \\ 0 & 1 & 0 & 0 & 0 & \cdots & 0 \\ 0 & 0 & 1 & 0 & 0 & \cdots & 0 \\ 0 & 0 & 0 & -\frac{Y_1}{c^2} & 1 & \cdots & 0 \\ \vdots & \vdots & \vdots & \vdots & \vdots & \ddots & \vdots \\ 0 & 0 & 0 & -\frac{Y_N}{c^2} & 0 & \cdots & 1 \end{pmatrix} \tag{37}$$

where $(\vec{n}, \vec{t_1}, \vec{t_2})$ is the basis normal to the boundary: $\vec{n} = n_x \vec{i} + n_y \vec{j} + n_z \vec{k}$ is the inward vector normal to the boundary and $\vec{t}_1 = t_{1_x} \vec{i} + t_{1_y} \vec{j} + t_{1_z} \vec{k}$ and $\vec{t}_2 = t_{2_x} \vec{i} + t_{2_y} \vec{j} + t_{2_z} \vec{k}$ are the tangential ones, e_c is the kinetic energy, $\hat{\gamma}(\beta) = \gamma - 1$, γ is the ratio between specific heat capacities

at constant volume and pressure:

$$\gamma = \frac{C_p}{C_v} \qquad C_v = \sum_{k=1,N} Y_k C_{vk} \qquad C_p = \sum_{k=1,N} Y_k C_{pk}$$

end χ_k is a parameter equal to:

$$\chi_k = r_k T - \beta e_{sk} \qquad e_{sk} = \int_0^T C_{vk} dT$$

where e_{sk} is the sensible energy of species k.

Acknowledgments

Figures

Case A

M_∞=0.028 and α=50%

t*=0	0.45	1.12	1.43

BC1

BC2

BC3
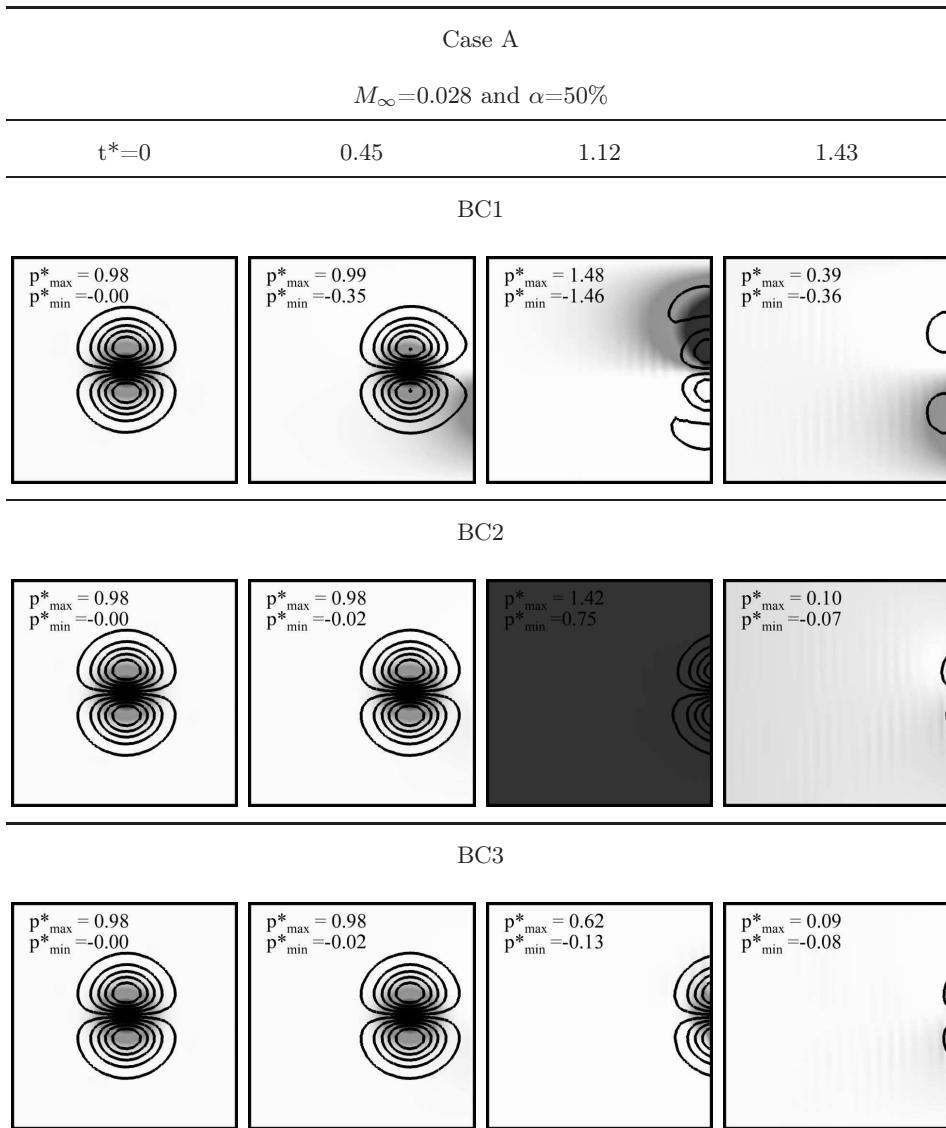
Fig. 1 Streamwise velocity isocontours and normalized pressure field p^* (gray scale) for case A. Frames are taken at four distinct dimensionless times (from left to right): t*=(0, 0.45, 1.12, 1.43).
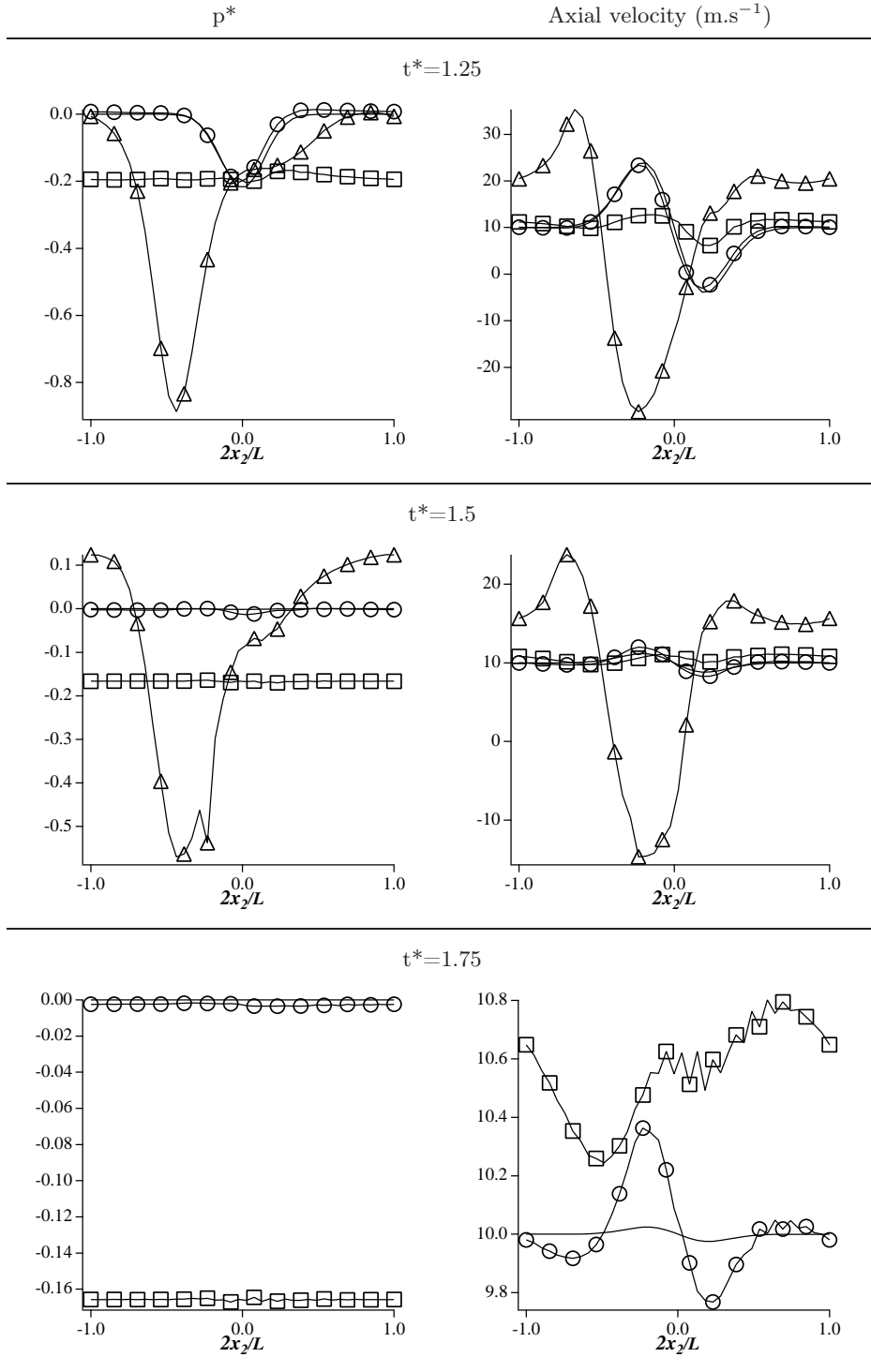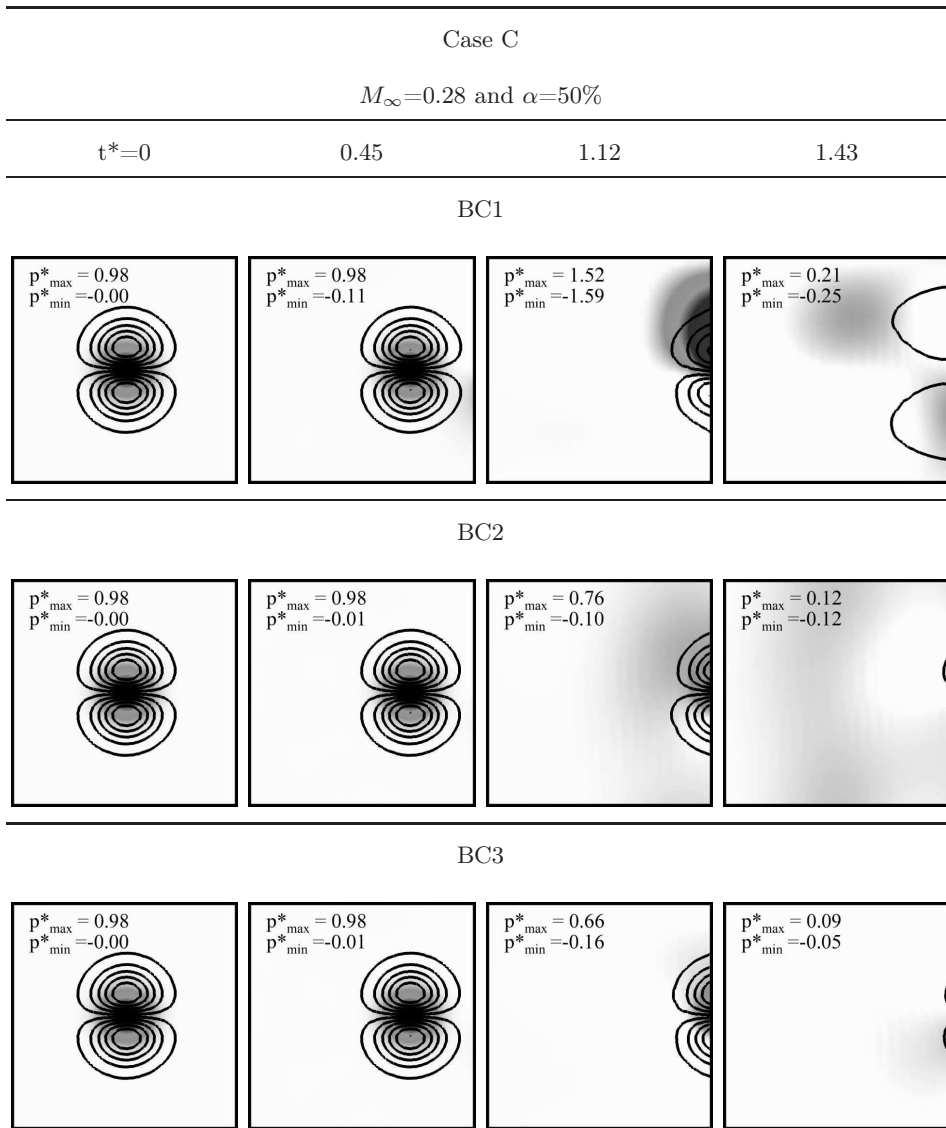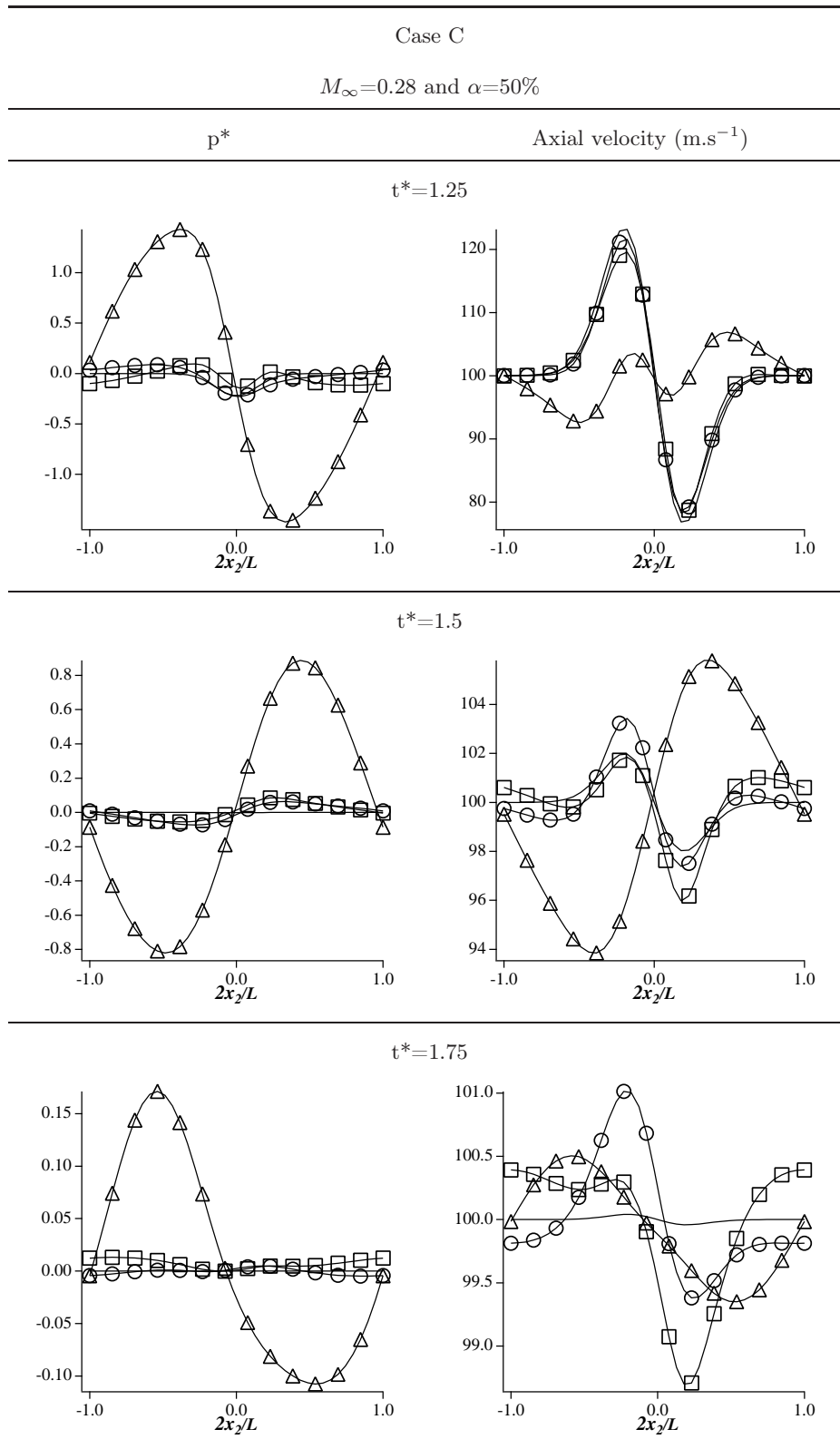
Case A

M_∞=0.028 and α=50%

p*	Axial velocity (m.s^{-1})

t*=1.25

t*=1.5

t*=1.75
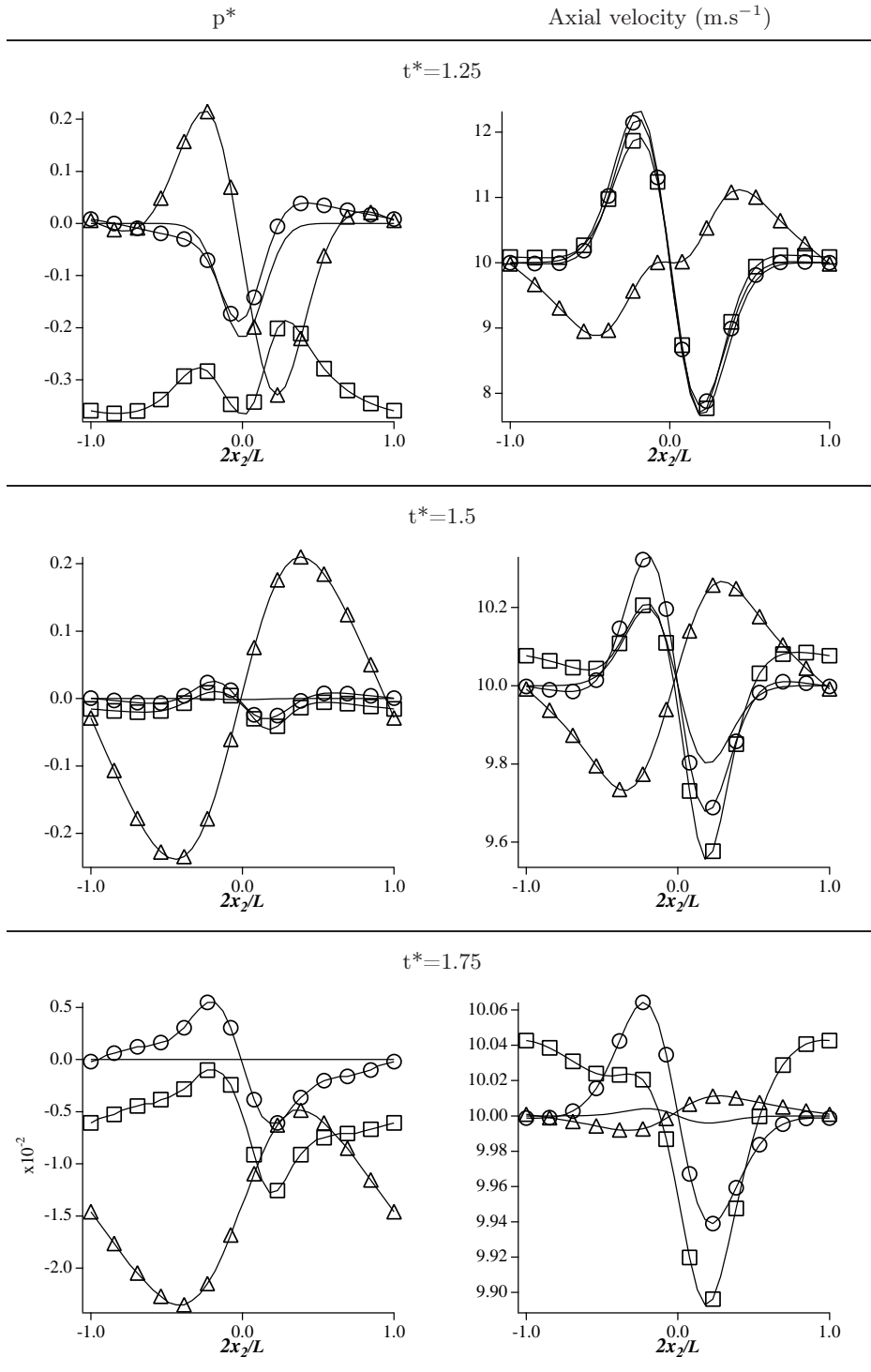
Fig. 2 Normalized pressure field (left column) and axial velocity (right column) plotted against distance x_2 at $x_1 = L/2$ for case A: ($\triangle$) BC1, ($\square$) BC2, (O) BC3, (-) Analytical solution.

Case B

M_∞=0.028 and α=300%

| t*=0 | 0.45 | 1.12 | 1.43 |

BC1

p^*_{max} = 0.98
p^*_{min} =-0.00

p^*_{max} = 0.98
p^*_{min} =-0.04

p^*_{max} = 0.82
p^*_{min} =-0.14

p^*_{max} = 0.86
p^*_{min} =-0.08

BC2

p^*_{max} = 0.98
p^*_{min} =-0.00

p^*_{max} = 0.98
p^*_{min} =-0.00

p^*_{max} = 0.41
p^*_{min} =0.23

p^*_{max} = 0.17
p^*_{min} =0.16

BC3

p^*_{max} = 0.98
p^*_{min} =-0.00

p^*_{max} = 0.98
p^*_{min} =-0.00

p^*_{max} = 0.66
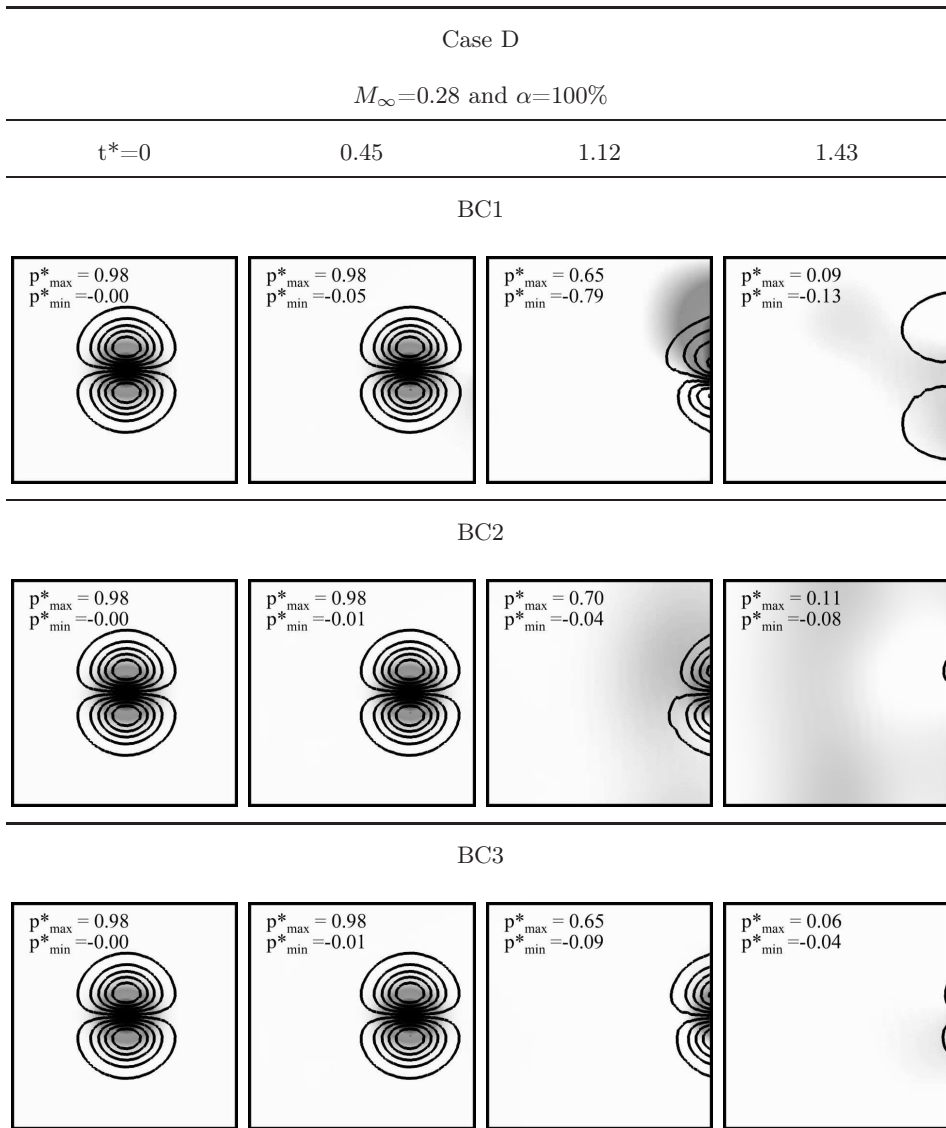p^*_{min} =-0.06

p^*_{max} = 0.03
p^*_{min} =-0.01
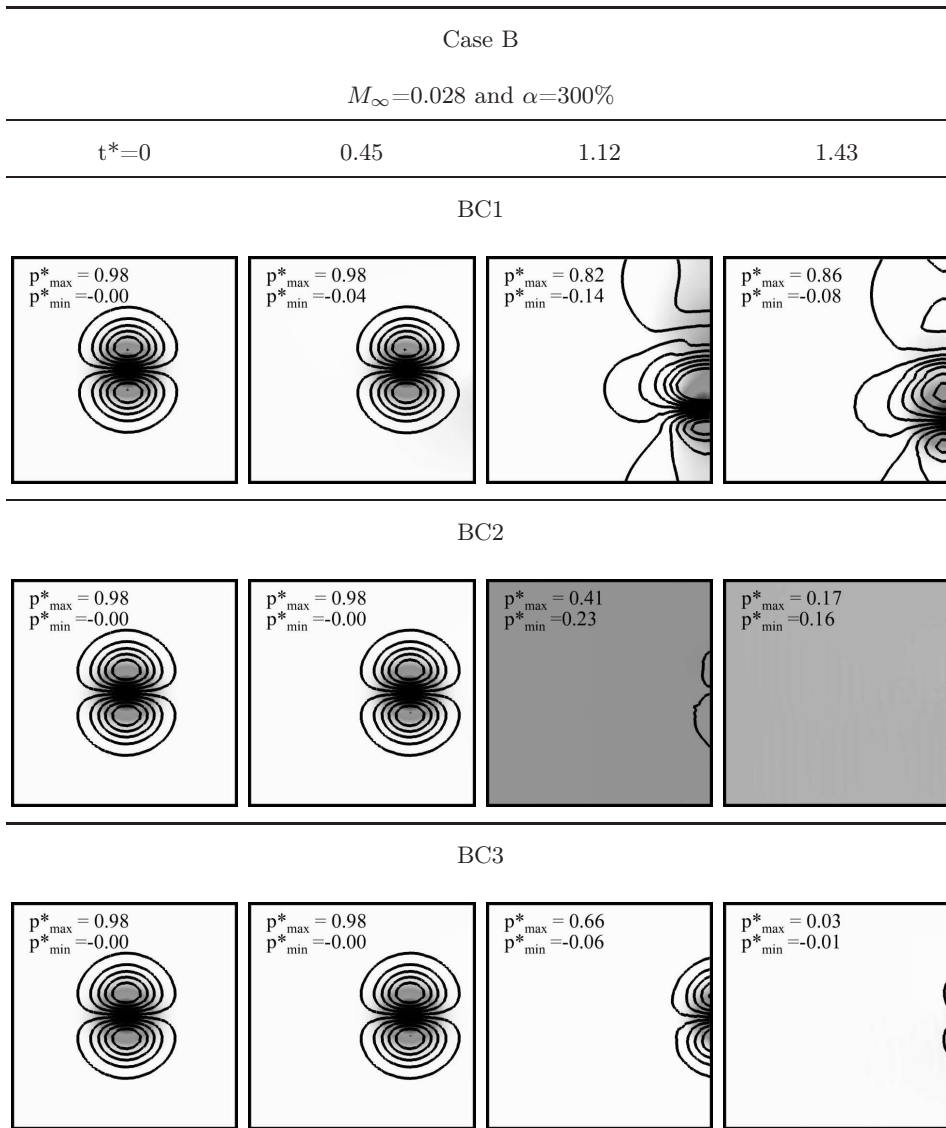
Fig. 3 Streamwise velocity isocontours and normalized pressure field p^* (gray scale) for case B. Frames are taken at four distinct dimensionless times (from left to right): t*=(0, 0.45, 1.12, 1.43).

Case B

$M_\infty = 0.028$ and $\alpha = 300\%$

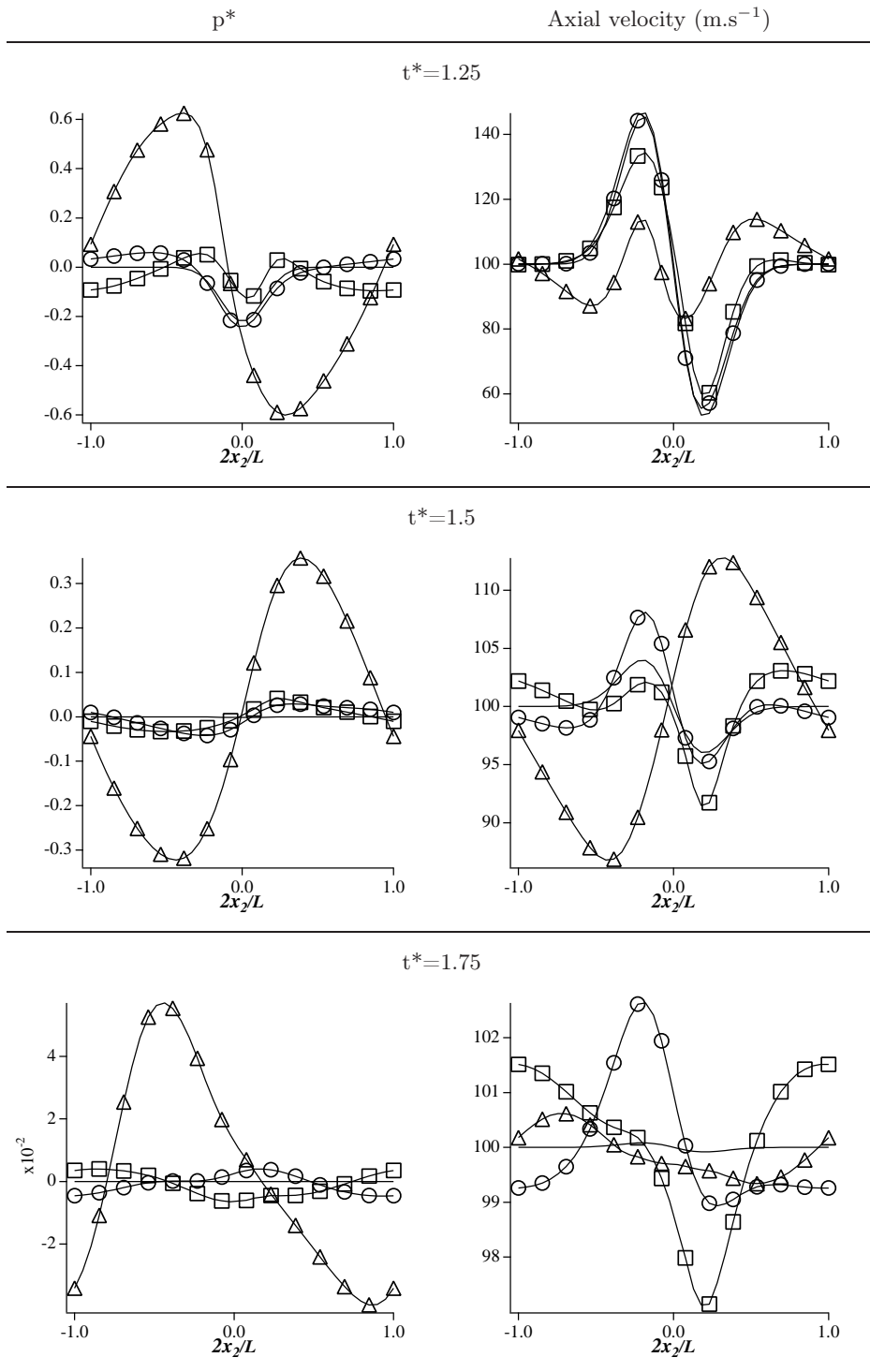| p*	Axial velocity (m.s^{-1})

t*=1.25

t*=1.5

t*=1.75

Fig. 4 Normalized pressure field (left column) and axial velocity (right column) plotted against distance x_2 at $x_1 = L/2$ for case B: ($\triangle$) BC1, ($\square$) BC2, (O) BC3, (-) Analytical solution.

Case C

M_∞=0.28 and α=50%

t*=0	0.45	1.12	1.43

BC1

BC2

BC3

Fig. 5 Streamwise velocity isocontours and normalized pressure field p^* (gray scale) for case C. Frames are taken at four distinct dimensionless times (from left to right): t*=(0, 0.45, 1.12, 1.43).

p*	Axial velocity (m.s^{-1})

t*=1.25

t*=1.5

t*=1.75

Fig. 6 Normalized pressure field (left column) and axial velocity (right column) plotted against distance x_2 at $x_1 = L/2$ for case C: ($\triangle$) BC1, ($\square$) BC2, (O) BC3, (-) Analytical solution.

Case D

M_∞=0.28 and α=100%

t*=0	0.45	1.12	1.43

BC1

BC2

BC3

Fig. 7 Streamwise velocity isocontours and normalized pressure field p^* (gray scale) for case D. Frames are taken at four distinct dimensionless times (from left to right): t*=(0, 0.45, 1.12, 1.43).

p*	Axial velocity (m.s^{-1})

t*=1.25

t*=1.5

t*=1.75

Fig. 8 Normalized pressure field (left column) and axial velocity (right column) plotted against distance x_2 at $x_1 = L/2$ for case D: ($\triangle$) BC1, ($\square$) BC2, (O) BC3, (-) Analytical solution.
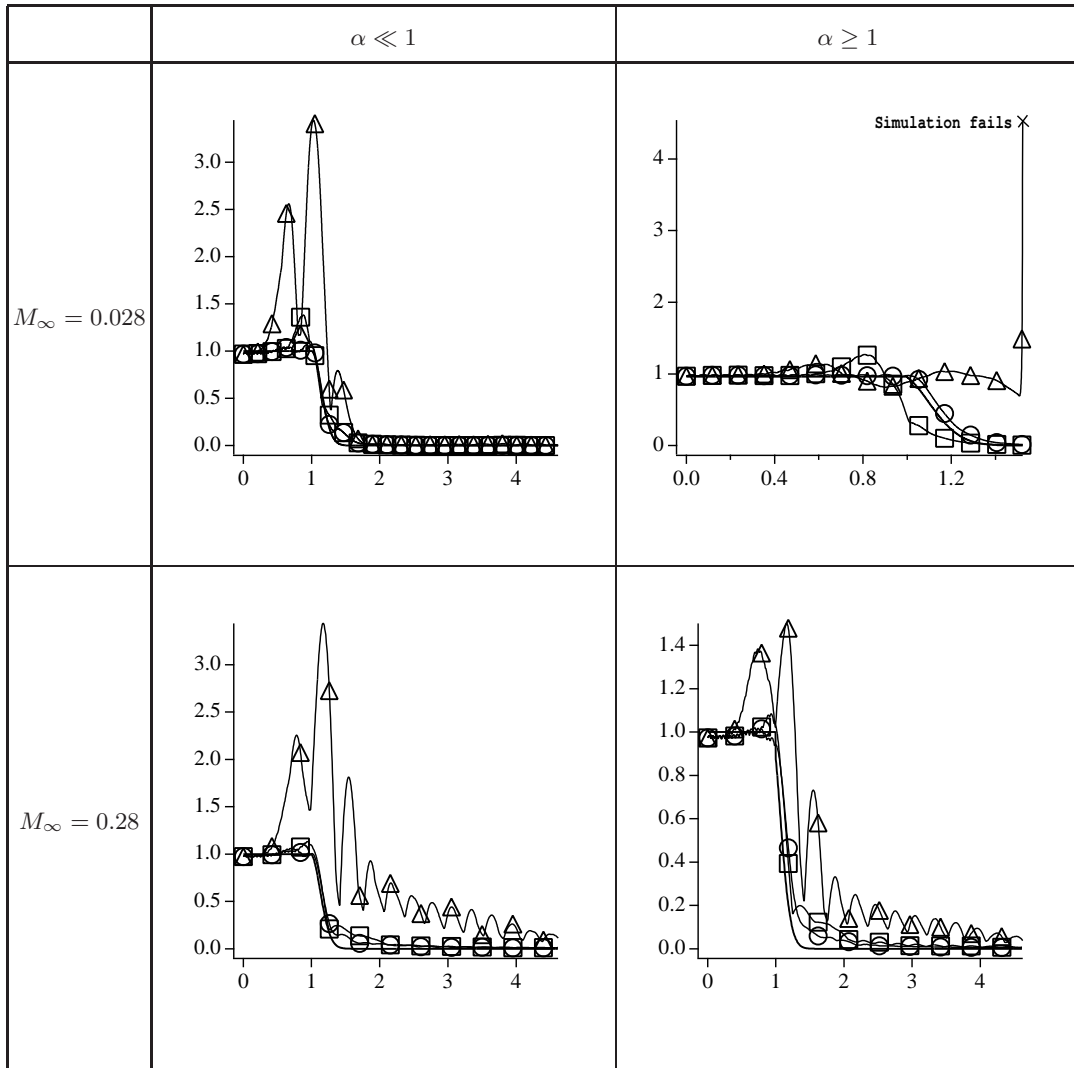
Fig. 9 Mean pressure in the whole domain (nondimensionalized by its initial value) versus the dimensionless time t^* for the four cases **A** (top left), **B** (top right), **C** (bottom left) and **D** (bottom right): ($\triangle$) BC1, ($\square$) BC2, (O) BC3, (-) Analytical solution.
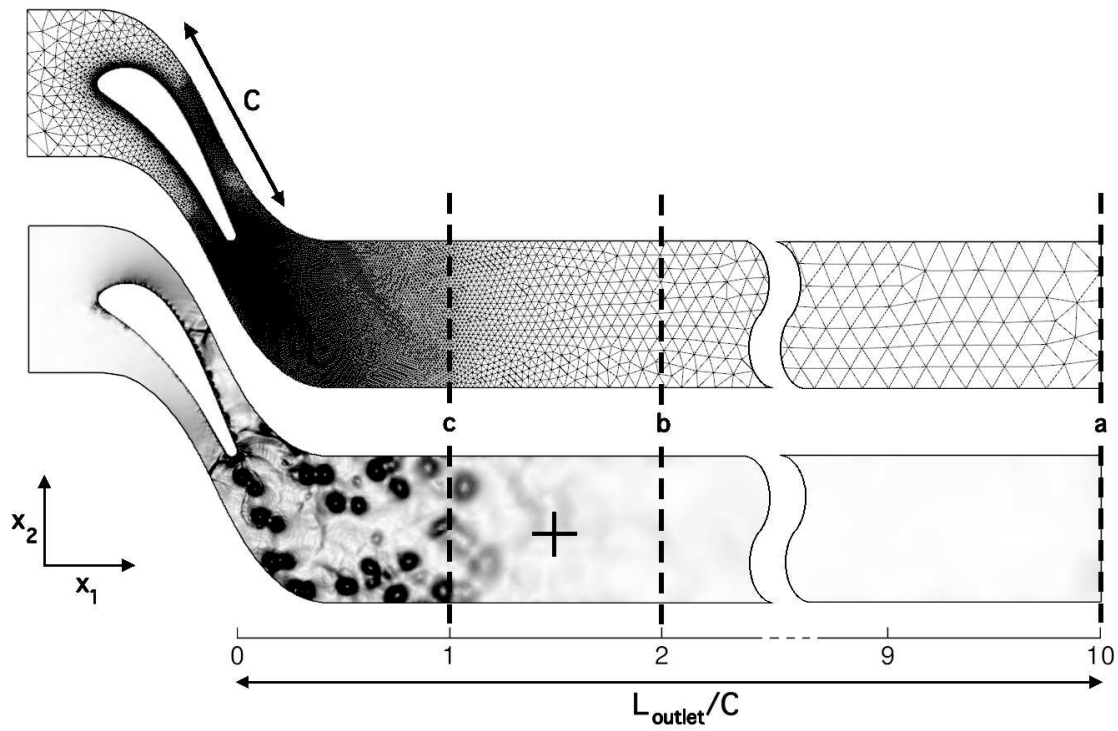
Fig. 10 Computational grid and field of $\nabla\rho$ for the reference case with an outlet boundary condition at 10 chords ($L_{outlet} = 10C$). The black cross indicates the location of the probe.
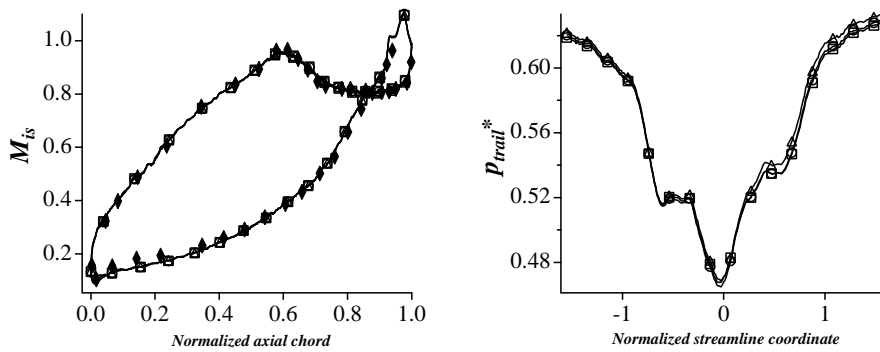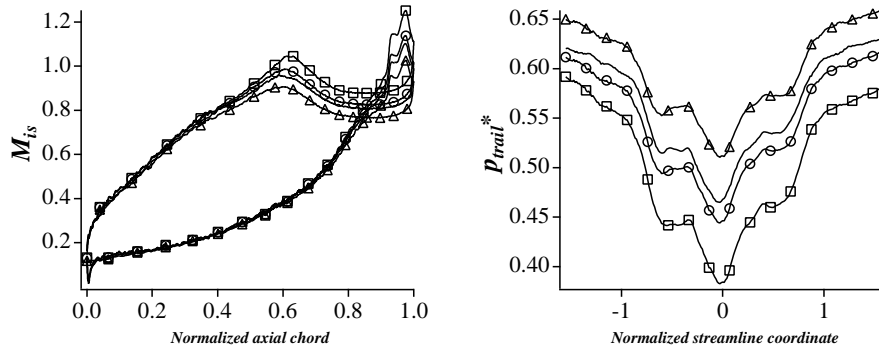

Fig. 11 Time-averaged isentropic Mach distribution along the blade wall (left) and time-averaged pressure distribution along the blade trailing edge normalized by the inlet pressure (right) for an outlet boundary condition located 10 chords away from the blade trailing edge compared to the experiment: ($\triangle$) BC1, ($\square$) BC2, (O) BC3, ($\blacklozenge$) Experiment.

Fig. 12 Time-averaged isentropic Mach distribution along the blade wall (left) and time-averaged pressure distribution along the blade trailing edge normalized by the inlet pressure (right) for an outlet boundary condition located **2** chords away from the blade trailing edge ($L_{outlet}/C = 2$): ($\triangle$) **BC1**, ($\square$) **BC2**, (**O**) **BC3**, (-) Reference simulation ($L_{outlet}/C = 10$).
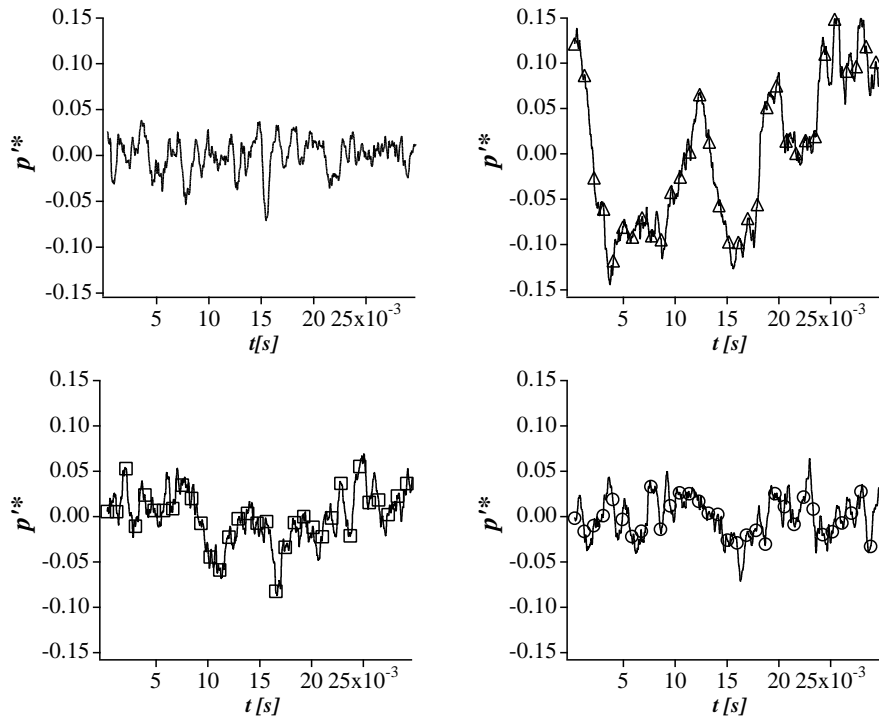

Fig. 13 Temporal evolution of the pressure fluctuation, normalized by the time-averaged pressure drop in the domain, at the probe shown in **Fig. 10** for the outlet boundary condition located **2** chords away from the blade trailing edge ($L_{outlet}/C = 2$): ($\triangle$) **BC1**, ($\square$) **BC2**, (**O**) **BC3**, (-) Reference simulation ($L_{outlet}/C = 10$).
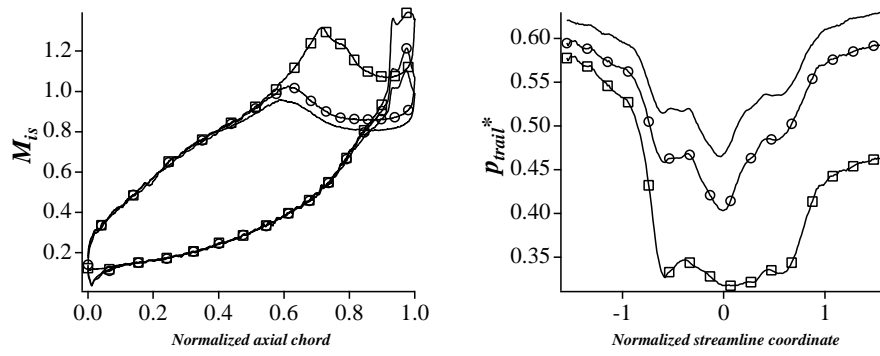
Fig. 14 Time-averaged isentropic Mach distribution along the blade wall (left) and time-averaged pressure distribution along the blade trailing edge normalized by the inlet pressure (right) for an outlet boundary condition located 1 chord away from the blade trailing edge ($L_{outlet}/C = 1$): ($\square$) BC2, (O) BC3, (-) Reference simulation ($L_{outlet}/C = 10$).

References

[1] Bogey, C. and Bailly, C., "Effects of inflow conditions and forcing on subsonic jet flows and noise," AIAA Journal, Vol. 43, No. 5, 2005, pp. 1000–1007.

[2] Bodony, D. J. and Lele, S. K., "On using Large-Eddy Simulation for the prediction of noise from cold and heated turbulent jets," Physics of Fluids, Vol. 17, 2005.

[3] Freund, J. B., "Noise sources in a low-Reynolds-number turbulent jet at Mach 0.9," Journal of Fluid Mechanics, Vol. 438, 2001, pp. 277–306.

[4] Buell, J. and Huerre, P., "Inflow outflow boundary conditions and global dynamics of spatial mixing layers," Proceedings of the Summer Program, Center for Turbulence Research, NASA Ames/Stanford Univ., 1988, pp. 19–27.

[5] Poinsot, T. and Veynante, D., Theoretical and Numerical Combustion, R.T. Edwards, 2nd edition, 2005.

[6] Hedstrom, G. W., "Non reflecting boundary conditions for nonlinear hyperbolic systems," Journal of Computational Physics, Vol. 30, 1979, pp. 222–237.

[7] Thompson, K. W., "Time dependent boundary conditions for hyperbolic systems," Journal of Computational Physics, Vol. 68, 1987, pp. 1–24.

[8] Hirsch, C., Numerical Computation of Internal and External Flows, John Wiley, New York, 1988.

[9] Poinsot, T. and Lele, S., "Boundary conditions for direct simulations of compressible viscous flows," Journal of Computational Physics, Vol. 101, No. 1, 1992, pp. 104–129.

[10] Prosser, R., "Improved Boundary conditions for the direct numerical simulation of turbulent subsonic flows I: Inviscid flows," Journal of Computational Physics, Vol. 207, 2005, pp. 736–768.

[11] Prosser, R., "Towards improved boundary conditions for the DNS and LES of turbulent subsonic flows," Journal of Computational Physics, Vol. 222, 2007, pp. 469–474.

[12] Yoo, C., Wang, Y., Trouvé, A., and Im, H., "Characteristic boundary conditions for direct simulations of turbulent counterflow flames," Combustion Theory and Modelling, Vol. 9, 2005, pp. 617–646.

[13] Yoo, C. and Im, H., "Characteristic boundary conditions for simulations of compressible reacting flows with multi-dimensional, viscous, and reaction effects," Combustion Theory and Modelling, Vol. 11, 2007, pp. 259–286.

[14] Lodato, G., Domingo, P., and Vervisch, L., "Three-dimensional boundary conditions for Direct and Large-Eddy Simulation of compressible viscous flow," Journal of Computational Physics, Vol. 227, No. 10, 2008, pp. 5105–5143.

[15] Baum, M., Poinsot, T. J., and Thévenin, D., "Accurate boundary conditions for multicomponent reac-

tive flows," Journal of Computational Physics, Vol. 116, 1994, pp. 247–261.

[16] Moureau, V., Lartigue, G., Sommerer, Y., Angelberger, C., Colin, O., and Poinsot, T., "Numerical methods for unsteady compressible multi-component reacting flows on fixed and moving grids," Journal of Computational Physics, Vol. 202, No. 2, 2005, pp. 710–736.

[17] Guezénnec, N. and Poinsot, T., "Acoustically Nonreflecting and Reflecting Boundary Conditions for Vorticity Injection in Compressible Solvers," AIAA, Vol. 47, No. 7, 2009, pp. 1709–1722.

[18] Vermorel, O., Richard, S., Colin, O., Angelberger, C., Benkenida, A., and Veynante, D., "Towards the understanding of cyclic variability in a spark ignited engine using multi-cycle LES," Combustion and Flame, Vol. 156, 2009, pp. 1525–1541.

[19] Schmitt, P., Poinsot, T., Schuermans, B., and Geigle, K. P., "Large-eddy simulation and experimental study of heat transfer, nitric oxide emissions and combustion instability in a swirled turbulent high-pressure burner," Journal of Fluid Mechanics, Vol. 570, 2007, pp. 17–46.

[20] Patel, N. and Menon, S., "Simulation of spray–turbulence–flame interactions in a lean direct injection combustor," Combustion and Flame, Vol. 153, No. 1-2, 2008, pp. 228–257.

[21] Nicoud, F., "Defining wave amplitude in characteristic boundary conditions," Journal of Computational Physics, Vol. 149, No. 2, 1998, pp. 418–422.

[22] Rudy, D. H. and Strikwerda, J. C., "A non-reflecting outflow boundary condition for subsonic Navier Stokes calculations," Journal of Computational Physics, Vol. 36, 1980, pp. 55–70.

[23] Sutherland, J. and Kennedy, C., "Improved boundary conditions for viscous, reacting, compressible flows," Journal of Computational Physics, Vol. 191, 2003, pp. 502–524.

[24] Liu, Q. and Vasilyev, O., "Nonreflecting boundary conditions based on nonlinear multidimensional characteristics," International Journal for Numerical Methods in Fluids, Vol. 62, No. 1, 2010, pp. 24–55.

[25] Colin, O., Simulations aux grandes échelles de la combustion turbulente prémélangée dans les statoréacteurs, Phd thesis, INP Toulouse, 2000.

[26] Schønfeld, T. and Rudgyard, M., "A cell-vertex approach to local mesh refinement for the 3-D Euler equations," 32nd Aerospace Sciences Meeting & Exhibit, AIAA Paper 1994-0318, Reno, U.S.A., 1994.

[27] Colin, O. and Rudgyard, M., "Development of high-order Taylor-Galerkin schemes for unsteady calculations," Journal of Computational Physics, Vol. 162, No. 2, 2000, pp. 338–371.

[28] Sieverding, C., Richard, H., and Desse, J.-M., "Turbine blade trailing edge flow characteristics at high subsonic outlet mach number," Transactions of the ASME, Vol. 125, 2003, pp. 298–309.

[29] Sieverding, C., Ottolia, D., Bagnera, C., Comadoro, A., Brouckaert, J.-F., and Desse, J.-M., "Unsteady

turbine blade wake characteristics," <u>Journal of Turbomachinery</u>, Vol. 126, 2004, pp. 551–559.